Doctor Thesis

Analysis of oscillatory rocking curve by dynamical diffraction in protein crystals

Ryo Suzuki

Graduate School of Nanobioscience,

Yokohama City University

30 November 2018

Preface

For practical materials such as Si and GaN, it has been widely recognized that the evaluation of the crystal perfection and fundamental physical properties is quite important for applications and product developments. In the particular case of protein crystals, it is important for both potential applications as novel biomaterials and structural analysis of protein molecules. However, the perfection and physical properties of protein crystals have scarcely been evaluated. This is due to that the growth of large and high-quality protein crystals is quite difficult, although various methods such as magnetic fields, microgravity have been developed to obtain the high-quality protein crystals so far.

For the assessment of crystal perfection, the observation of dynamical X-ray diffraction in crystalline materials is an interesting question since it is an evidence for the perfect crystals. However, there is no report on the observation of clear dynamical diffraction in protein crystals yet while the crystallization methods of the high-quality protein crystals have been developed. There are some mysteries whether the crystal perfection of high-quality protein crystals is still low compared with that of high-quality crystals such as Si, or protein crystals cannot produce the clear dynamical diffraction in principle. It has been a long-standing important issue in the fields of structural biology and diffraction physics.

While the crystal perfection in protein crystals has been investigated, the studies on the mechanical properties of protein crystal have been performed by a few research groups so far. However, none of

them has provided the dislocation behaviors due to the difficulty of the growth of high quality crystals and the brittleness of protein crystals under the stresses. To develop the innovative applications, the elucidation of the mechanical properties has been desired.

In this thesis, the evaluation of the dynamical X-ray diffraction and the mechanical properties of high-quality protein crystals were carried out using synchrotron X-ray topography. The oscillatory profile of rocking curves for protein crystals such as glucose isomerase is observed. In addition, the stress-induced defects, especially dislocations, are characterized as the physical property in protein crystals.

This thesis is composed of 5 chapters. In Chapter 1, the general introduction and the background of this study is described. Chapter 2 deals with the preparation method of the high-quality glucose isomerase crystals. In Chapter 3, it is described “Analysis of oscillatory rocking curve by dynamical diffraction in protein crystals”. In Chapter 4, it is described “Direct observation of stress-induced dislocations in protein crystals by synchrotron X-ray topography”. Finally, general discussion and conclusion are given in Chapter 5.

Most of this thesis has been published in the following journals;

1. R. Suzuki, H. Koizumi, K. Hirano, T. Kumasaka, K. Kojima, M. Tachibana,

   Analysis of oscillatory rocking curve by dynamical diffraction in protein crystals.

   Proceedings of the National Academy of Sciences of the United States of America **115** (2018) 3634–3639.

2. R. Suzuki, M. Tachibana, H. Koizumi, K. Kojima,

   Direct observation of stress-induced dislocations in protein crystals by synchrotron X-ray topography.

   Acta Materialia **156** (2018) 479–485.

Finally, I am glad if this study becomes the key for big applications.

Ryo Suzuki

Yokohama, Japan

November 2018

Table of Contents

Chapter 1

General Introduction

1.1 Purpose of the thesis

It is important to understand the structures of protein molecules in order to elucidate the life phenomena and drug discovery. The three-dimensional structures of various protein molecules have been revealed by X-ray diffraction using protein crystals so far. The accuracy of the structure obtained by X-ray diffraction strongly depends on the crystal perfection. Therefore, various crystallization methods such as magnetic fields, microgravity, electric fields have been suggested to obtain the high-quality protein crystals [1].

Protein crystals are composed of huge protein molecules with complex shapes. The molecular size is an order of nanometer as compared with that of angstrom for common crystals. In addition, they contain a large amount of water with 20 to 70 vol.% [2,3]. The interactions between the protein molecules are quite weaker and complex. Moreover, the properties of protein crystals are comparable to porous materials such as typical zeolites and porous silica [4–6]. These features are much different from the common inorganic and organic crystals. It is expected that protein crystals give rise to unique physical properties.

It is a well-known fact that in the case of semiconductor materials typified Si and the blue light emitting diodes of GaN, the development of high-quality crystals and the measurement of their

fundamental physical properties such as mechanical, thermal, electrical, magnetic and optical properties are quite important for practical applications. On the other hand, in the case of protein crystals, it is important for both potential applications as novel biomaterials and hybrid devices, and structural analysis of protein molecules. However, first of all, the perfection and physical properties of protein crystals have scarcely been evaluated. This is due to that the growth of large and high-quality protein crystals is quite difficult. In order to elucidate the intrinsic physical properties of protein crystals, high-quality crystals of proteins are necessary.

In general, crystal perfection can be evaluated by X-ray diffraction. As shown in Figure 1.1, there are two principal theories such as kinematical and dynamical diffraction of X-ray [7–10]. Kinematical diffraction is a phenomenon in which X-ray scattering occurs once in a crystal. Such kinematical diffraction occurs in imperfect crystals *i.e.* crystals containing many defects and periodicity disordered. The ideal crystal model in kinematical diffraction is called as mosaic crystal as seen in Figure 1.1 (a).

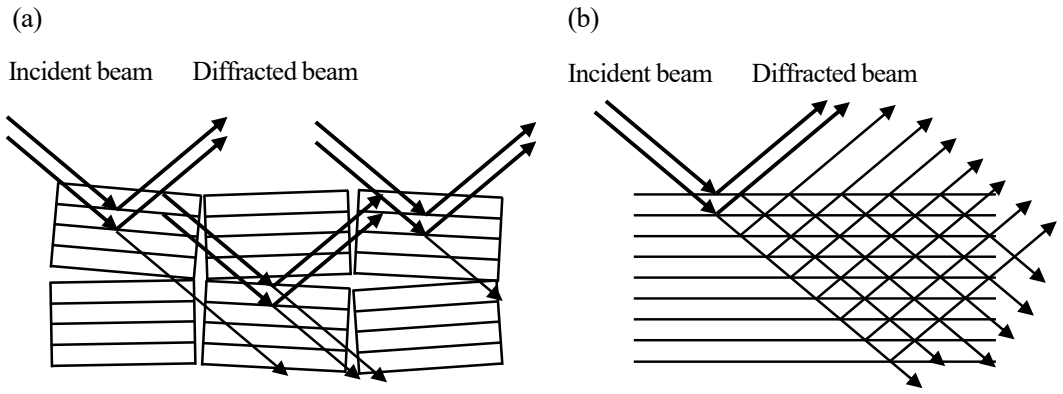

Figure 1.1. Schematic of (a) kinematical diffraction in mosaic crystal and (b) dynamical diffraction in perfect crystals.

On the other hand, dynamical diffraction is a phenomenon that multiple scattering of X-ray occurs in the crystal as seen in Figure 1.1 (b). Such dynamical diffraction occurs in ideal perfect crystals. In consideration of the crystal quality, all crystals exist between mosaic and perfect crystals depending on the degree of the crystal perfection. Therefore, an observation of dynamical X-ray diffraction is an indicator of the crystal perfection. As shown in Figure 1.2, dynamical diffraction can appear in extremely high-quality or almost perfect crystals as the Pendellösung fringes in wedge-shaped crystals by X-ray topography [11,12], the oscillatory profiles of rocking curves [13–16] in Si crystals, the maximum reflecting power as a function of the crystals thickness in Ge crystals [17], and the contrasts of stacking-fault fringes in diamond crystals [18]. Thus, dynamical diffraction can appear only perfect crystals. However, there is no report on the observation of clear dynamical diffraction in protein crystals yet while the crystallization method of the high-quality protein crystals has been developed. There are some mysteries whether the crystal perfection of high-quality protein crystals is still low compared with that of high-quality semiconductor crystals, or protein crystals cannot produce the clear dynamical diffraction in principle. It has been a long-standing important issue in the fields of structural biology and diffraction physics.

The physical properties of materials are closely related to crystal perfection. In order to understand the physical properties, especially mechanical properties, it is most important to evaluate crystal defects, especially, the dislocations behavior [19]. The dislocations affect the mechanical properties of

the crystalline materials. The mechanical properties and the relationship between dislocations and deformations have been studied on various kinds of materials such as inorganic crystals and organic crystals with low molecular weight for a long time [20–25]. However, the mechanical properties of protein crystals have not been fully elucidated yet. The researches on the mechanical properties are limited in number due to the difficulty of the crystallization and handling of protein crystals. Even if protein crystals with large size are obtained, it is hard to identify the defects in the low-quality crystals.

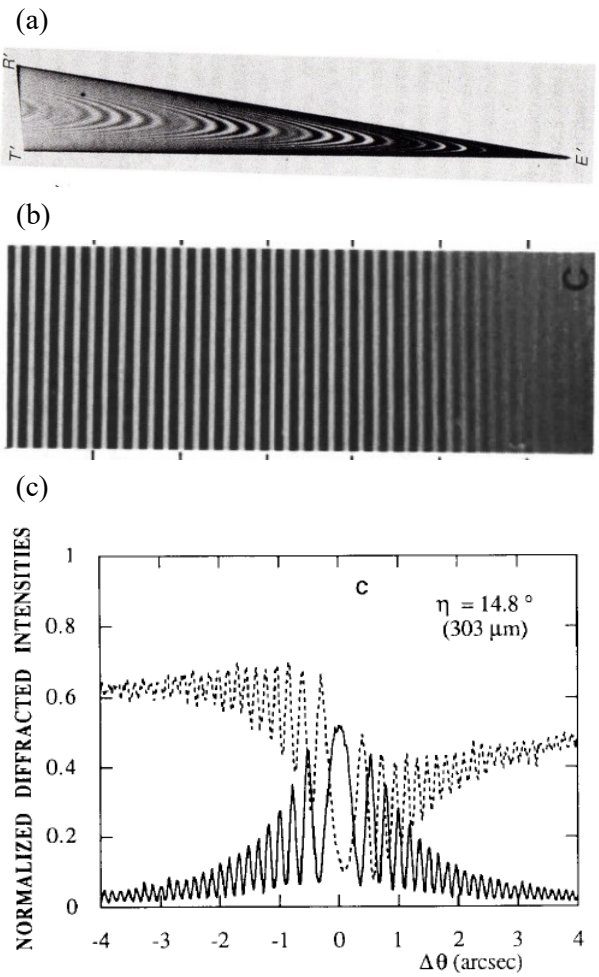

Figure 1.2. (a,b) Pendellösung fringes and the equal-thickness fringes in wedge-shaped Si crystals [11,15] and (c) the oscillatory profiles of rocking curves in Si crystals [16].

The elucidation of the intrinsic mechanical properties such as dislocation behavior has been desired using high-quality protein crystals. Therefore, growth of large size and high-quality protein crystals, and evaluation of the fundamental physical properties are most important question to apply the protein crystals as novel materials.

1.2 History of studies on perfection and mechanical properties of protein crystals

X-ray topography is one of the most powerful non-destructive method for the identification of crystal perfection and crystal defects, especially, dislocations in crystals [10,26–28]. In the case of protein crystals, it is difficult to identify the crystal perfection by electron microscope due to the intra-crystalline water. Since 1995, many research groups have carried out the studies on crystal perfection of protein crystals, mainly hen egg-white lysozyme (HEWL) crystals, by synchrotron X-ray topography [29–44]. However, the topographic contrasts of crystal defects in protein crystals are poor compared to those seen for common inorganic and organic with small molecule crystals as shown in Figure 1.3(a-e). The poor contrasts can be attributed to not only the poor crystal quality but also the submillimeter crystal size which is smaller than the lower limit crystal thickness of typical protein crystals for kinematic contrasts, *i.e.* direct images, in X-ray topography [26,28,45]. On the other hand, the clear topographic contrasts for millimeter size HEWL crystals have been obtained by synchrotron monochromatic-beam X-ray topography as shown in Figure 1.3(f) [46–48]. The crystal defects,

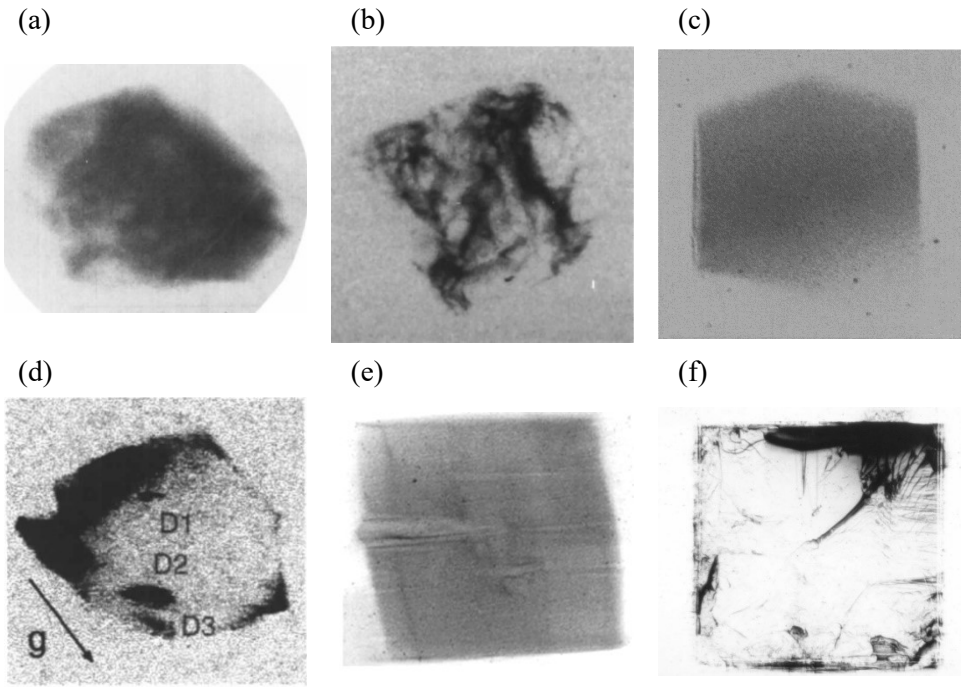

Figure 1.3. X-ray topographs of tetragonal HEWL crystals [29,30,32,37,40,47].

especially dislocations, have been characterized and the Burgers vectors have also been identified in HEWL crystals with polymorphisms [46–48].

As mentioned above, various crystallization methods of high-quality protein crystals meant for X-ray structural analysis have been suggested [1]. Some X-ray topographic experiments for HEWL crystals [34], ferritin crystals [38], and glucose isomerase (GI) crystals [49,50] (which is described at Appendix A in this thesis) showed fringe contrasts similar to Pendellösung fringes in part of the crystal as shown in Figure 1.4. From these studies, dynamical diffraction in protein crystals has been expected although the related studies do not provide a quantitative explanation to support this premise. On the other hand, rocking curve measurements have been also performed for several protein crystals [51–

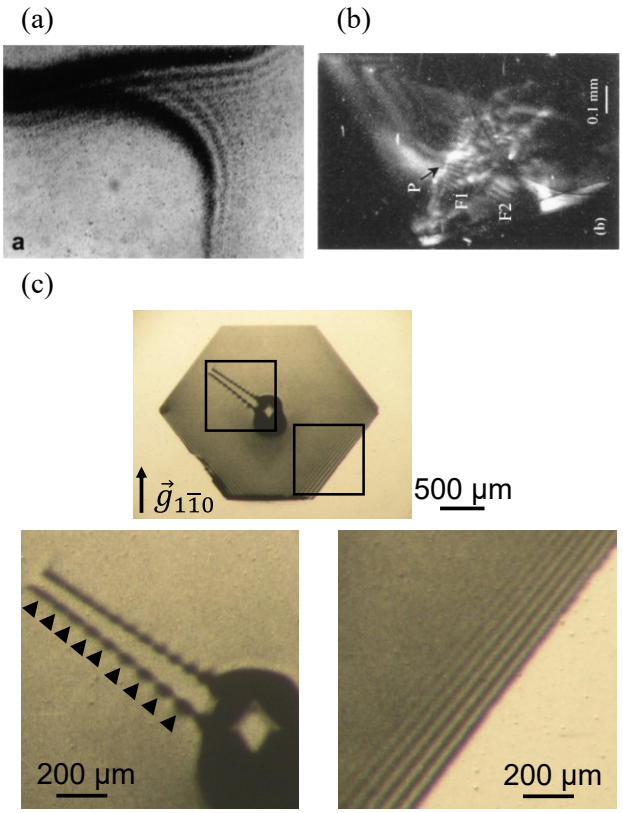

Figure 1.4. X-ray topographs of (a) tetragonal HEWL crystals, (b) ferritin crystals and (c) glucose isomerase crystals [34,38,50].

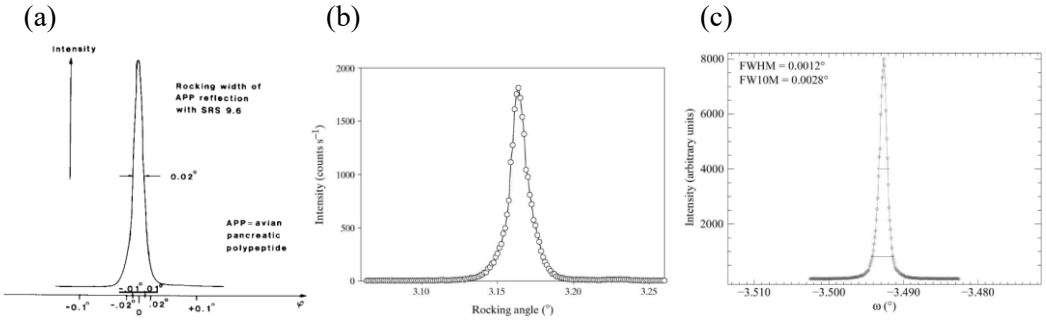

Figure 1.5. The rocking curve profiles of HEWL crystals [51,53,54].

54]. However, as shown in Figure 1.5, there is no report showing clear dynamical diffraction such as oscillatory rocking curves in protein crystals yet.

While the crystal defects in protein crystals have been investigated, the studies on the mechanical properties of protein crystal have been performed by a few research groups. Almost all of them have

been carried out on HEWL crystals with polymorphisms. Micro-Vickers hardness tests with the indentation have been mainly performed on tetragonal and orthorhombic HEWL crystals [55–59]. It has been considered that the plastic deformation by the indentation is due to the dislocation mechanism even in protein crystals. As shown in Figure 1.6, it has been presumed from the observation of slip traces after the indentation [55–59]. According to previous reports, protein crystals exhibit much low shear modulus, C_{44}, compared with common ionic, metal and covalent crystals as seen in Table 1.1 [60,61]. This suggests that the dislocations are easily introduced by an applied stress. However, there is no report yet on direct observation of stress-induced dislocations in protein crystals. This is due to the difficulty of the growth of large-size and high-quality crystals and the brittleness of protein crystals under the stresses.

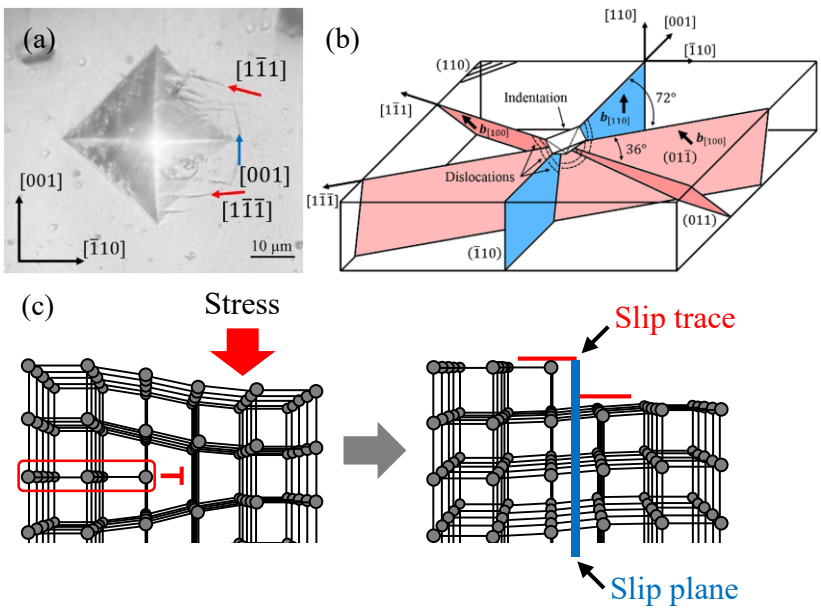

Figure 1.6. (a) The indentation mark and slip traces on HEWL crystals by the indentation [58], (b) schematic of the slip systems [58], and (c) schematic of slip deformation.

Table 1.1. Comparison of the elastic constants of protein crystals with those of other crystals [60,61].

Crystal	Bonding	C_{11} [GPa]	C_{44} [GPa]
Orthorhombic HEWL	*H, V, I*	5.24	0.30
Tetragonal HEWL	*H, V, I*	5.50	0.68
Benzophenone	*V*	10.8	2.10
H_2O (ice)	*H*	15.3	4.46
NaCl	*I*	48.7	12.6
Cu	*M*	168	75.4
Si	*C*	165	79.6

H: hydrogen bonds, *V*: van der Waals bonds, *I*; ionic bonds, *M*: metallic bonds, and *C*: covalent bonds.

1.3 Outline of the thesis

In this thesis, the subjects are as follows; one is the perfection of high-quality protein crystals and the other is the mechanical properties of high-quality protein crystals. The crystal perfection and plastic deformation mechanisms of glucose isomerase (GI) crystals which is one of the enzyme proteins were examined using X-ray topography and the indentation method in this study. The outline of each chapter is as follows.

The preparation of large-size and high-quality GI crystals is shown in Chapter 2. The high-quality GI crystals with large-size are grown using seed crystals. Protein crystals are quite brittle and fragile. The preparation of seed crystals and transfer to the growth solution is most important process. Even when high-quality protein crystals are obtained, it is difficult to set up the specimens for X-ray topographic observation and indentation test. The measurement of the crystal perfection without

handling damage is important. To easily grow high-quality crystals with large-size and improve the setup of the crystals, crystallization skills and special specimen holders were established.

The crystal perfection of GI crystals is investigated in Chapter 3. The perfection was evaluated by rocking curve measurement using X-ray topography. As a result, the oscillatory profiles of rocking curves were observed. The oscillatory profiles show good agreement with that predicted by the dynamical theory of X-ray diffraction. It is demonstrated that dynamical diffraction occurs in protein crystals, as Si. These results indicate the possibility of the perfect crystals of proteins. They also suggest the need for a dynamical diffraction model in protein-crystal structural analysis and model refinement which has never been used in conventional structural analysis. Moreover, the evaluation of the fundamental physical properties of protein crystals is much expected using such perfect crystals.

In chapter 4, the measurement of mechanical properties of high-quality GI crystals by indentation test and the observation using X-ray topography are performed. Although past studies have suggested the existence of the stress-induced dislocations, none of them has provided direct observation of the dislocations due to the difficulty of the growth of high quality crystals and the brittleness of protein crystals under the stresses. The observation of dislocations which were induced by the indentation method in defect-free GI crystals were succeeded. The characters of stress-induced dislocations in protein crystals as similar to those in inorganic crystals, which can become the basis for the practical applications of protein crystals.

Finally, the intrinsic perfection and mechanical properties of protein crystals are discussed in Chapter 5.

1.4 Integrated Science and the thesis

Protein crystals are mainly investigated in the field of bioscience. In general, however, protein crystals are just one of the structural analysis tools to obtain the three-dimensional structure of protein molecules. The solid-state physics in protein crystals are novel fields of science since it has mainly dealt with inorganic and organic materials so far. It is quite important to establish and develop the solid-state physics in protein crystals. When one has succeeded, protein crystals can be applied for novel energy devices, hybridization with other materials and drug design by the structural analysis of protein molecules with higher resolution. Therefore, this thesis focuses on the crystal perfection and the mechanical properties in protein crystals. In the future, this study surely play an essential role in the novel materials application and high-resolution structural analysis.

Chapter 2

Preparation of high-quality glucose isomerase crystals with large-size

The phenomenon of protein lysis and precipitation is a result of which of the interaction of protein-solvent molecules, and the interaction of protein-protein molecules prevailed. In general, protein crystals are obtained in an aqueous solution. A technique using a salt or an organic solvent as a precipitant is used for protein crystallization. By depriving the activity of water molecules bounded to the surface of protein molecules, the interaction between protein molecules is strengthened. As a result, protein molecules are arranged periodically and they form a crystal.

Protein crystals are quite brittle and fragile compared with ordinary materials. Even if the protein crystals are obtained, researchers often break the protein crystals in their own hands accidentally. In order to measure the intrinsic crystal perfection and physical properties, it is important to treat the crystals without handling damage and touching directly. Therefore, in this study, a special crystal holder was developed. The special crystal holder is established by siliconized cover glass, acrylic holder and plastic cover slide. The siliconized cover glasses and plastic cover slides were purchased from Hampton Research. They are useful for avoiding the heterogeneous nucleation. The acrylic holder was designed as shown in Figure 2.1. Using this special crystal holder, it is possible to grow and set up the crystal without handling damage for X-ray topographic measurement and the

indentation test.

The solution of glucose isomerase (GI) from *Streptomyces rubiginosus* was purchased from Hampton Research. The glucose isomerase solution was used without further purification after filtering with pore size of 0.1 μm. The glucose isomerase crystals were grown by using seed crystals. First, the seed crystals were grown from a crystallization solution containing 33 mg/mL glucose isomerase, 6 mM tris(hydroxymethyl)-aminomethane (TRIS) hydrochloride (pH 7.0), 0.91 M ammonium sulfate, and 1 mM magnesium sulfate by hanging drop vapor diffusion technique. The technique is a popular method to crystallize the macromolecules. A drop composed of crystallization solution is placed in vapor equilibration with a reservoir liquid. As water leaves the drop, the concentration of protein and precipitants increases in relative supersaturation. As a result, the crystallization occurs gradually and the crystal size reaches around 100 μm. In this experiment, the amounts of the drop solution and reservoir solution are 20 μm and 1 mL, respectively. After 1~2 days, the seed crystals were obtained. The seed crystal was pick up without a few damages using CryoLoop (Hampton Research) with nylon. After that, the seed crystal put in a crystallization droplet on the

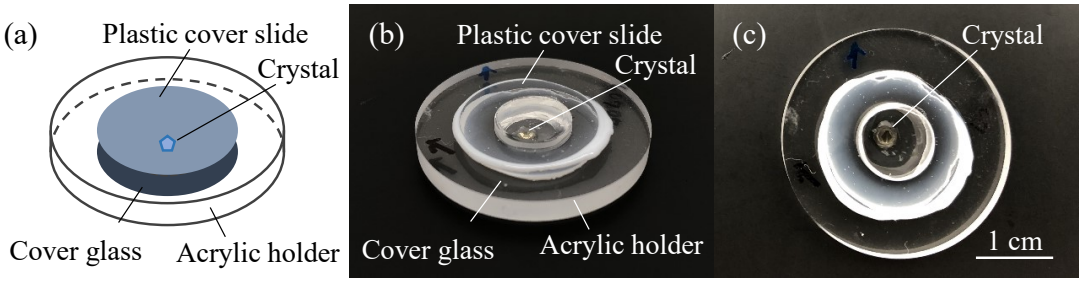

Figure 2.1. (a) A schematic figure and (b,c) photographs of oblique and top view of a special crystal holder, respectively.

siliconized cover glass (Hampton Research) attached with a special crystal holder as shown in Figure 2.2 (a). The droplet is the same solution as that for the growth of the seed crystals as mentioned above. To avoid the heterogeneous nucleation in the droplet, the crystal holder containing the droplet and seed crystal was annealed at 40 ºC for 30 min. After the annealing, the crystal holder was covered with plastic cover slides (Hampton Research) and kept at 20 ºC. After 2 weeks, the grown crystals with large-size were obtained as shown in Figure 2.2 (b).

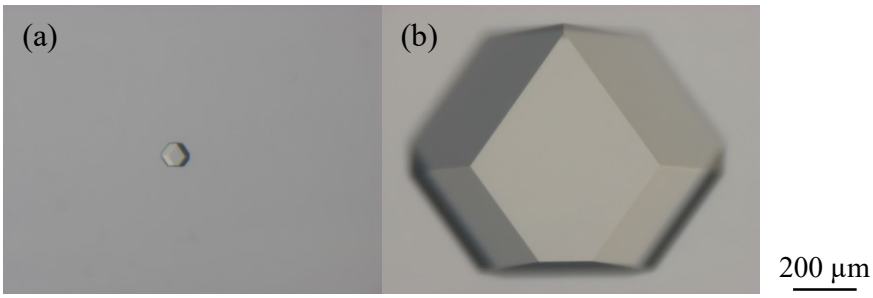

Figure 2.2. (a) A typical seed crystal and (b) the grown crystal of glucose isomerase after 2 weeks.

Chapter 3

Analysis of oscillatory rocking curve by dynamical diffraction in protein crystals

Abstract

High-quality protein crystals meant for structural analysis by X-ray diffraction have been grown by various methods. The observation of dynamical diffraction in protein crystals is an interesting topic because dynamical diffraction generally occurs in perfect crystals such as Si crystals. However, there is no report yet on protein crystals showing clear dynamical diffraction. We wonder whether the perfection of protein crystals might still be low compared with that of high-quality Si crystals. Here, we present the first observation of the oscillatory profile of rocking curves for protein crystals such as glucose isomerase crystals. The oscillatory profiles are in good agreement with those predicted by the dynamical theory of diffraction. We demonstrate that dynamical diffraction occurs even in protein crystals. This suggests the possibility of the use of dynamical diffraction for the determination of the structure and charge density of proteins.

3.1 Introduction

The observation of dynamical X-ray diffraction in protein crystals is an interesting topic for the

assessment of crystal perfection and the structural analysis of proteins. Generally, there are two principal theories—kinematical and dynamical—associated with X-ray diffraction in crystals [7–10]. The kinematical theory treats the scattering from each volume element in the crystal sample as being independent of other elements. Therefore, kinematical diffraction commonly occurs in small crystals or low-quality crystals with defects such as dislocations. On the other hand, the dynamical theory takes into account multiple scattering within the crystal and is generally used whenever diffraction from a large perfect crystal is considered. Even in small crystals, dynamical diffraction is often encountered while measuring a strong reflection, which is usually a low-order reflection associated with a large structure factor. Thus, dynamical diffraction is an indicator of the perfection of crystals. Dynamical diffraction can appear in high-quality covalent crystals as the Pendellösung fringes in wedge-shaped crystals during X-ray topography [11,12], the oscillatory profiles of rocking curves [13–16] in Si crystals, the maximum reflecting power as a function of the crystal thickness in Ge crystals [17], and the contrasts of stacking-fault fringes in diamond crystals [18].

High-quality protein crystals meant for structural analysis by X-ray diffraction have been grown by various methods including gel and microgravity growth [1]. However, there is no report showing clear dynamical diffraction in protein crystals yet. We wonder whether the perfection of protein crystals is still low compared with that of high-quality Si crystals. Protein crystallographers assume based on kinematical theory that the diffraction intensity is proportional to the magnitude of the structure factor

squared [62]. Some X-ray topographic experiments for hen egg-white lysozyme (HEWL) [34], ferritin [38], and glucose isomerase (GI) crystals [49] showed fringe contrasts similar to Pendellösung fringes in part of the crystal. A recent report also showed bead-like or oscillatory contrasts along dislocation images in X-ray topographs [50]. These topographic images are similar to typical images of dynamical diffraction [10, 63]. From these observations, it is expected that dynamical diffraction might occur in protein crystals, although the related studies do not provide a quantitative explanation to support this premise. On the other hand, rocking curve measurements have been performed for several protein crystals [51–54]. However, there is no report on the observation of the oscillatory profile associated with dynamical diffraction. In this study, we present the first observation of the oscillatory profiles of rocking curves in protein crystals such as GI crystals. The oscillatory profiles are in good agreement with those predicted by the dynamical theory of diffraction. It is demonstrated that dynamical diffraction, which is usually seen in high-quality Si crystals, occurs even in protein crystals.

3.2 Materials and Methods

3.2.1 Crystal growth

The solution of GI from *Streptomyces rubiginosus* was purchased from Hampton Research Corp. and used without further purification. The crystallization conditions were the same as those mentioned in previous reports [49,50]. The GI crystals were grown using macroseeds. Their thicknesses ranged from

approximately 200 to 800 μm, where they were measured using an optical microscope. The crystal belonged to the orthorhombic space group of *I*222 with lattice constants of a = 93.88 Å, b = 99.64 Å, and c = 102.90 Å and contained two tetrameric molecules per unit cell [64]. The crystals were bounded by the $\{110\}$, $\{101\}$, and $\{011\}$ crystallographic faces, as shown in Figure 3.2 (b). For X-ray diffraction experiments such as X-ray topography and rocking curve measurements, the grown GI crystals were sealed in an acrylic cell, as has been reported previously [49,50].

3.2.2 Rocking curve measurement

The rocking curve measurements with X-ray topography were performed at room temperature in BL20B at the Photon Factory (PF) of the High Energy Accelerator Research Organization (KEK). The rocking curves were obtained in the Laue geometry configuration. A two-crystal monochromator consisting of a Si(111) crystal was placed 11 m from the source and was used to select the X-ray wavelengths of interest. The monochromatic beams of λ = 1.0 Å, 1.2 Å, and 1.4 Å without focusing were selected as the incident beams in this work. Note that the beam intensity is considerably low compared with conventional beam intensities at beam lines used for protein-structure analysis at synchrotron radiation facilities.

The incident beam with a size of 3 × 5 mm^2 covering an entire crystal sample was introduced almost perpendicular to the $(0\bar{1}1)$ or (101) plane of the crystal sample, which was mounted on a precision

goniometer and was rotated with a high-resolution angular step (minimum angular step width: 0.19 arcsec (5.3×10^{-5}°)) around the exact Bragg angle of the reflected wave. A schematic of the experimental setup with crystal mounting is shown in Figure 3.1. The crystal thickness was almost perpendicular to the beam path. The scattering plane was perpendicular to the polarization direction of the incident beam. Under such conditions, the reflected images of the entire crystal corresponding to the angular steps were collected using a high-spatial-resolution, two-dimensional, digital CCD camera (Photonic Science X-RAY FDI 1.00:1, effective pixel size: 6.45×6.45 μm^2) with exposure times of approximately 4 min. The reflected images from the CCD camera correspond to digital X-ray topographs. The conventional high-resolution X-ray topographs were obtained by using X-ray films with exposure times of approximately 2 min in place of the CCD camera.

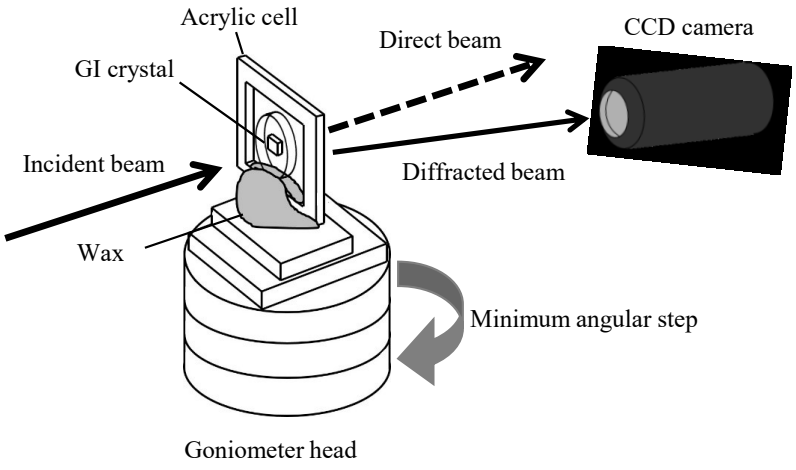

Figure 3.1. Schematic of the experimental setup with crystal mounting for rocking curve measurements with X-ray topography in BL20B at KEK-PF. The crystal sample in an acrylic cell was mounted on the goniometer and was rotated with a high-resolution angular step (minimum angular step width: 0.19 arcsec (5.3×10^{-5}°)) around the exact Bragg angle of the reflected wave.

The dose of a 4-min exposure for the acquisition of a series of reflected images as mentioned above is approximately 0.05 kGy, which is considerably lower than the conventional dose of 500 kGy used for protein-structure analysis at room temperature at synchrotron radiation facilities [51,65,66]. However, a longer exposure of about 120 min even with a low beam intensity caused radiation damage that led to a change in the rocking curves. This means that the rocking curve profile is sensitive to the crystal quality and radiation damage. To avoid radiation damage, short exposure times less than 20 min for each crystal sample, corresponding to a dose of less than 0.24 kGy, were used in the X-ray diffraction experiments.

X-ray rocking curve profiles were reconstructed from the reflected intensities in a selected circular area with a diameter of 96.75 μm (15 pixels) of the crystal image that corresponds to the effective beam spot size. Note that the size was determined by the effective size, which is sufficient to delineate the rocking curve using the reflected intensities.

Similar rocking curve measurements were also carried out in BL38B1 at SPring-8, in which the X-ray topographic system for protein crystals is under construction.

3.3.3 Angular resolution of the optics

To measure the rocking curves of the crystal samples, the angular resolution of the optics must be less than or equal to the intrinsic FWHM of the rocking curve predicted by dynamical theory. The angular

resolution of the optics, φ, which is the instrumental resolution function, can be estimated by using the following equation obtained from the Drummond diagram [68] and the geometry of the experimental system:

$$\varphi = \left(1 - \frac{\tan\theta_2}{\tan\theta_1}\right)\min\left[\Delta\theta, \sigma_{y'}\right] + \frac{\tan\theta_2}{\tan\theta_1}\omega, \tag{3.1}$$

where

$$\Delta\theta = 2\tan^{-1}\left(\frac{2\sigma_y\sqrt{2\ln 2} + s}{2L}\right), \tag{3.2}$$

$$\omega = \frac{2}{\pi}\frac{r_e}{V_c}\frac{|F|\lambda^2}{\sin 2\theta_B}. \tag{3.3}$$

θ_1 and θ_2 are the Bragg angles for the monochromator crystal and crystal sample, respectively. $\Delta\theta$ is the beam divergence estimated from the geometry of the experimental system, $\sigma_{y'}$ is the vertical beam divergence, and ω is the intrinsic FWHM of the rocking curve. σ_y is the vertical beam size, s is the slit size, and L is the distance between the light source and the X-ray detector, which is the CCD camera.

At BL20B in the PF, $\Delta\theta$ was calculated to be 3.39 arcsec (9.41×10^{-4}°) using Eq. (3.2) with L = 14.35 m; σ_y = 0.059 mm, as shown in the facility status of the PF [68]; and s = 96.75 μm, which is the effective spot size mentioned above. For the 111 reflection of the Si crystal used as the monochromator in BL20B in the PF, ω was calculated to be 3.99 arcsec (1.11×10^{-3}°) from Eq. (3.3) with V_c = 1.60×10^{-28} m^3, $|F|$ = 45.0465 (Crystallography Open Database: 4507226), and θ_B = 11.03° with λ = 1.2 Å. Using these values of $\Delta\theta$ and ω, the angular resolution of the optics φ was

evaluated to be 2.54 arcsec (7.06×10^{-4}°) from Eq. (3.1) with θ_1 = 11.03°, θ_2 = 0.480° with λ = 1.2 Å, and $\sigma_{y'}$ = 2.48 arcsec (6.88×10^{-4}°), as shown in the facility status of the PF [68].

The intrinsic FWHM of the rocking curve of the 011 reflection for GI crystals was also estimated from Eq. (3.3) with $|F|$ = 14,380 (PDB ID: 1mnz) [69], V_c = 9.63×10^{-25} m^3, and θ_B = 0.480° with λ = 1.2 Å. As a result, the FWHM was calculated to be 4.75 arcsec (1.32×10^{-3}°). This value was larger than φ corresponding to the angular resolution of the optics as estimated above. This implies that the intrinsic FWHM for GI crystals can be well-resolved in BL20B.

On the other hand, the intrinsic FWHM of the rocking curve for tetragonal HEWL crystals, which are often used as model protein crystals, was calculated to be 0.42 arcsec (1.17×10^{-4}°) from Eq. (3.1) for a typical 440 reflection with an incident beam with a wavelength of 1.2 Å. The value of the intrinsic rocking width was smaller than φ = 2.81 arcsec (7.80×10^{-4}°) of the angular resolution of the optics for tetragonal HEWL crystals in BL20B as mentioned above. In this case, resolving the intrinsic rocking curve profiles for tetragonal HEWL crystals might be difficult. Therefore, GI crystals would be more suitable for the study of the dynamical diffraction of protein crystals in BL20B.

3.3 Results and Discussion

Figures 3.2 (a) and (b) show an optical micrograph of a typical GI crystal and the corresponding schematic figure, respectively. The digital X-ray topographs and rocking curves of such GI crystals of

different sizes were measured by using a high-resolution charge-coupled device (CCD) camera. Figure 3.2 (c) shows a typical digital X-ray topograph for the same crystal as that in Figure 3.2 (a). As seen in Figure 3.2 (c), no dislocations are visible in the crystal. This means that dislocation-free GI crystals of high quality are obtained in this experiment. Additionally, it is confirmed that no clear change in the X-ray topographic image is observed before and after the rocking curve measurement (Figure 3.3). Even in the high-resolution X-ray topographs taken with X-ray films, no crystal defects such as dislocations are observed after the rocking curve measurement (Figure 3.4). These results suggest that the X-ray exposure for the rocking curve measurement in this experiment gives rise to no significant damage such as the generation of dislocations. Moreover, it should be noted that fringe contrasts similar to Pendellösung fringes exhibiting a high crystal quality, as reported previously [49,50], are clearly observed at the tapered or wedge-like edges of the crystals in the X-ray topographs. The fringe contrasts seem to depend on the angular dispersion of the beam and the beam coherence [15]. Thus,

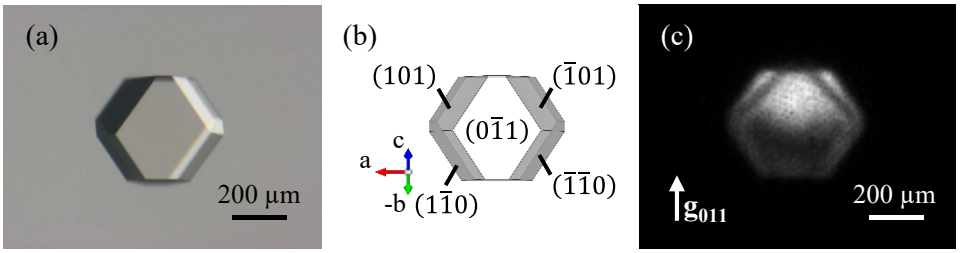

Figure 3.2. Typical GI crystal viewed from the crystallographic direction perpendicular to the $(0\bar{1}1)$ plane. (a) Optical micrograph, (b) corresponding schematic prepared with VESTA software [76], and (c) digital X-ray topograph with the CCD camera in BL20B at KEK-PF. No line contrasts corresponding to dislocations are observed in the X-ray topograph, whereas fringe contrasts similar to Pendellösung fringes exhibiting a high crystal quality seem to be observed at the tapered or wedge-like edges of the crystal.

dislocation-free GI crystals of high quality are retained even after the rocking curve measurements in this experiment.

Figure 3.5 shows a typical rocking curve profile of a GI crystal taken with the 011 reflection. The thickness of the GI crystal is 199 μm. The horizontal axis is called the W scale [10], which is the parameter representing the deviation from the diffraction condition given by

$$W = \frac{2\Lambda \sin\theta_B}{\lambda}(\theta_B - \theta), \tag{3.4}$$

where

$$\Lambda = \xi = \frac{\pi}{r_e}\frac{V_c}{\lambda}\frac{\cos\theta_B}{|F|}. \tag{3.5}$$

Λ and ξ are the periods of the Pendellösung fringes and the extinction distance in the Laue (transmission) case, respectively. θ_B is the Bragg angle, λ is the wavelength of the incident beam,

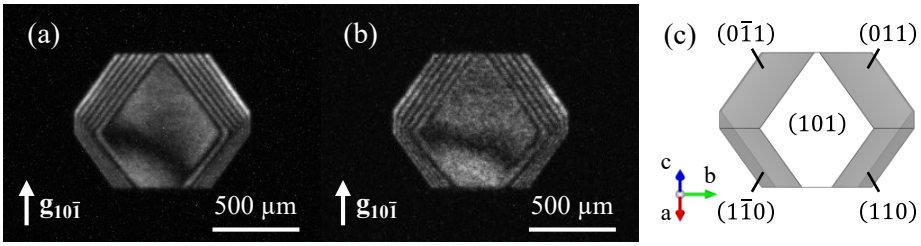

Figure 3.3. Digital X-ray topographs of a GI crystal taken (a) before and (b) after the rocking curve measurement in BL38B1 at SPring-8. The corresponding schematic of the crystal in (c) is drawn with VESTA software [76]. The incident beam is almost perpendicular to the $(\mathbf{101})$ plane, which is different from $(\mathbf{0\bar{1}1})$ in Figure 3.2 (a). No clear change in the X-ray topographic image is observed in (a) and (b). Namely, there are no line contrasts corresponding to dislocations. This means that the X-ray exposure for the rocking curve measurement gives rise to no significant damage such as the generation of dislocations. Additionally, it should be noted that fringe contrasts similar to Pendellösung fringes exhibiting a high crystal quality are observed at the tapered or wedge-like edges of the crystal. The fringe contrasts seem to depend on the angular dispersion of the beam and the beam coherence [15]. These X-ray topographic images show that dislocation-free high-quality crystals are maintained even after the rocking curve measurements.

V_c is the volume of the unit cell, r_e is the classical electron radius (2.82 × 10^{-15} m), and F is the structure factor. W for the 011 reflection of the GI crystal in Figure 1 is obtained from Eq. (3.4) with θ_B = 0.480°, λ = 1.2 Å, and Λ = 621 μm, which is calculated from Eq. (3.5) using V_c = 9.63 × 10^{-25} m^3 and $|F|$ = 14,380 (Protein Data Bank ID: 1mnz) [69].

It should be noted that a fine structure corresponding to oscillation is clearly observed on the wings of the rocking curve. To further explain the oscillation, the intensity of the rockin g curve shown on a linear scale in Figure 3.5 (a) is redrawn on a logarithmic scale, as sho wn in Figure 3.5 (b). The oscillatory profile is more clearly observed with the logarithmic s cale. Similar oscillatory rocking curves are also obtained from any circular areas with a dia

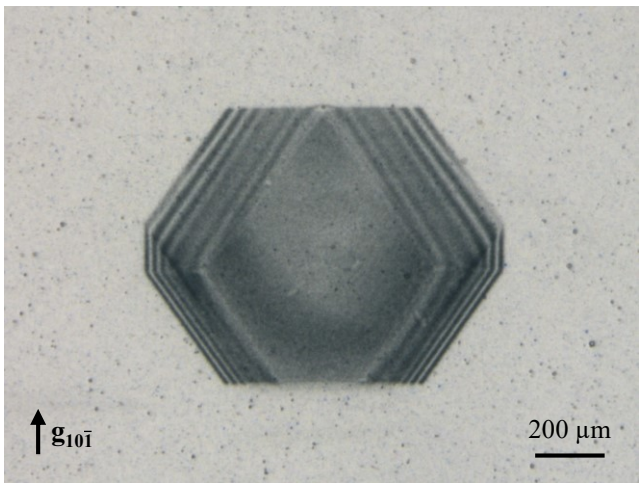

Figure 3.4. High-resolution X-ray topograph corresponding to the digital one in Figure 3.3 (b) after the rocking curve measurement, taken with X-ray film in BL38B1 at SPring-8. The X-ray topographic image with the X-ray film is similar to that with the CCD camera in Figure 3.3 (b). Even in the high-resolution X-ray topograph, no crystal defects such as dislocations are observed. Additionally, fringe contrasts similar to Pendellösung fringes exhibiting a high crystal quality are more clearly observed at the tapered or wedge-like edges of the crystal, as in Figure 3.3. This also means that dislocation-free high-quality crystals are retained even after the rocking curve measurements.

meter of 96.75 μm in the crystal, as shown in Figure 3.6. However, the corresponding Brag g angle θ_B is slightly shifted from one end part of the crystal to the other end by only app roximately 0.001°, which is very small and comparable to the angular resolution limit of the apparatus. This means that the crystal includes small distortion overall in spite of the fact t hat it is dislocation-free as mentioned above. As a result, even the small distortion perturbs the rocking curve profile of the whole crystal. Thus, clear oscillatory rocking curves are obt ained from not the overall area but smaller areas with a diameter of 96.75 μm in the crysta l as mentioned above. The series of X-ray topographic images associated with the oscillatory rocking curve are shown in supplementary video 1 (described in http://www.pnas.org/content /suppl/2018/03/19/1720098115.DCSupplemental).

It is well-known from the dynamical theory of diffraction that rocking curves exhibit such oscillatory profiles for perfect crystals [7–10]. Therefore, it is suggested that the oscillatory profiles

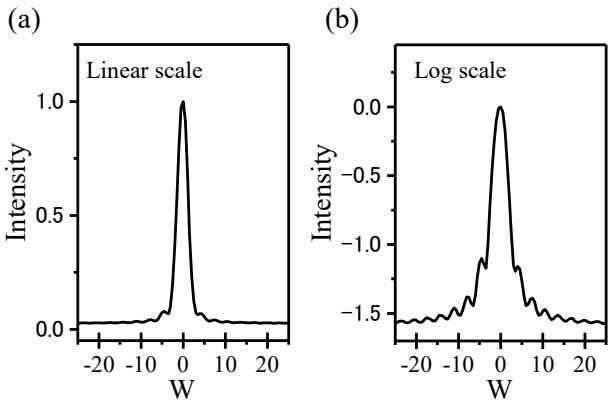

Figure 3.5. Typical rocking curve for the 011 reflection of a GI crystal with a thickness of 199 μm, taken with an incident beam with a wavelength of 1.2 Å in BL20B at KEK-PF. In (a) and (b), the intensities of the same rocking curves are shown on linear and logarithmic scales, respectively.

observed in the present experiments can be attributed to the dynamical effect of perfect crystals. This is the first observation of the dynamical effect in the rocking curves of protein crystals. Such a dynamical effect has been observed in only high-quality crystals such as Si crystals so far. This implies that it is possible to grow high-quality crystals similar to Si crystals using protein crystals with huge and complex molecules, although the perfect region is smaller than that in Si crystals.

According to the dynamical theory of diffraction with no absorption [10], the intrinsic rocking curve profile in the symmetric Laue case is given by

$$\frac{{I_g}^n}{I_o} = \frac{\sin^2\left(\pi H\sqrt{W^2+1}/\Lambda\right)}{W^2+1}, \tag{3.6}$$

where H is the crystal thickness. Both W and Λ in Eq. (3.6) are expressed as a function of the wavelength of the incident beam λ, according to Eqs. (3.4) and (3.5), respectively. From Eq. (3.6), it is found that the period of oscillation in the rocking curve depends on the wavelength of the incident

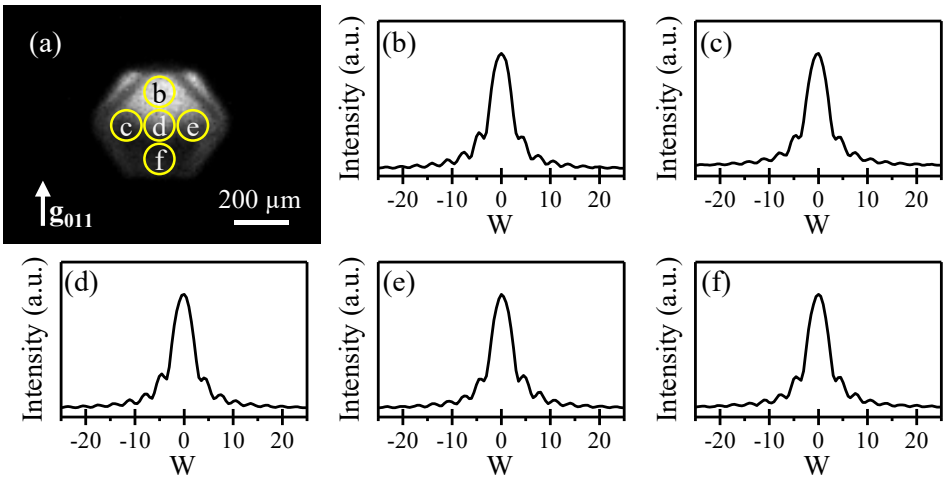

Figure 3.6. (a) Selected circular areas with a diameter of 96.75 μm (15 pixels) on a typical crystal image for rocking curves. (b–f) The rocking curve profiles are reconstructed from the reflected intensities in the selected areas. Similar oscillatory profiles of rocking curves are obtained from different sites.

beam. Therefore, to demonstrate the dynamical effect for the oscillatory profiles as suggested above, the rocking curves for the same GI crystal were measured using incident beams of different wavelengths. Figure 3.7 (a) shows the rocking curves of 011 reflections for the same GI crystals, taken with different wavelengths of 1.0 Å, 1.2 Å, and 1.4 Å, where the crystal thickness is 199 μm. As seen in Figure 3.7 (a), the period of oscillation decreases with the increasing wavelength of the incident beam. The wavelength dependence of the period of oscillation in the rocking curves is in good agreement with that predicted from Eq. (3.6). This supports the premise that the oscillatory profile measured in the present experiments can be attributed to the dynamical effect of diffraction.

Moreover, theoretical rocking curves based on the dynamical theory of diffraction with no absorption were calculated from Eq. (3.6) and compared with the measured values as mentioned above. The calculated curves for wavelengths of 1.0 Å, 1.2 Å, and 1.4 Å are shown in Figure 3.7 (b). As seen

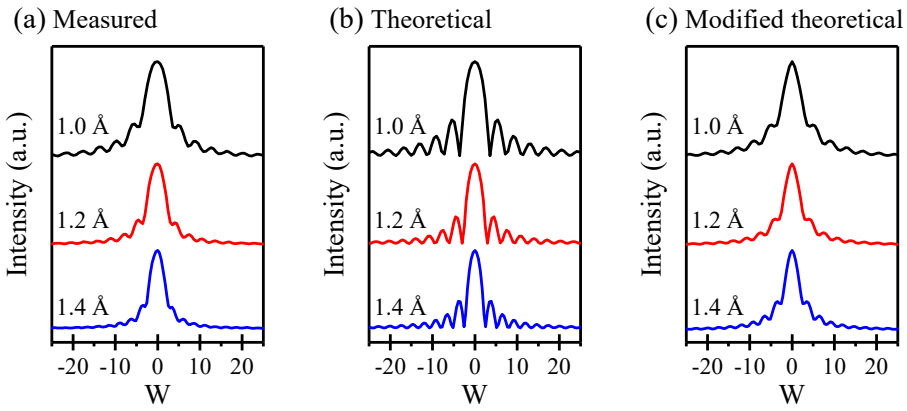

Figure 3.7. Rocking curves for 011 reflections of the same GI crystals with a thickness of 199 μm, taken with incident beams with different wavelengths of 1.0 Å, 1.2 Å, and 1.4 Å, in BL20B at KEK-PF. (a) Measured rocking curves, (b) theoretical rocking curves, and (c) modified theoretical rocking curves with the average one.

in Figure 3.7 (b), the periods of oscillations are in good agreement with the measured values, although the accuracy of the curve fitting is poor.

To improve the curve fitting, the average curve with no absorption [10] is added along with a ratio to Eq. (3.6), where the average curve is given by

$$\frac{\bar{I}_g{}^n}{I_o} = \frac{1}{2(W^2+1)}. \tag{3.7}$$

Therefore, the measured rocking curves were fitted with the modified theoretical curves given as follows:

$$I = r\frac{I_g{}^n}{I_o} + (1-r)\frac{\bar{I}_g{}^n}{I_o}, \tag{3.8}$$

where r is the ratio of $\frac{I_g{}^n}{I_o}$ to $\frac{\bar{I}_g{}^n}{I_o}$ with $0 \le r \le 1$. The ratio, $1-r$, of the average curve corresponds to the degree of smearing or background in the oscillatory curve, which originates from the resolution limit due to the angular divergence of the beam [14,15]. Note that the oscillatory periods of the calculated curves are independent of the corrections using the average curves. The calculated curves are shown in Figure 3.7 (c), where the values of r for λ = 1.0 Å, λ = 1.2 Å, and λ = 1.4 Å are 0.35, 0.33, and 0.38, respectively. As seen in Figure 3.7 (c), the modified theoretical curves are in good agreement with the measured curves. Thus, it is concluded that dynamical diffraction occurs even in protein crystals such as GI crystals.

Nevertheless, it is known that kinematical diffraction occurs when a crystal is sufficiently thin, irrespective of whether the crystal is perfect or not. Therefore, one might expect that kinematical

diffraction predominantly occurs for the thin crystal with a thickness of 199 μm, which is only one third of Pendellösung thickness. However, the rocking curve profile for the 199-μm-thick crystal predicted from kinematical theory is quite different from the measured rocking curve, as shown in Figure 3.8. Namely, the full width at half maximum (FWHM) obtained by using kinematical theory is two orders smaller than that of the measured rocking curve, as presented in Table 3.1. Thus, the measured rocking curve obtained in this work is not explained by kinematical diffraction.

Furthermore, rocking curves were also measured for GI crystals of different thicknesses. According to Eq. (3.6), the period of oscillation in the rocking curves decreases as the thickness of the crystals

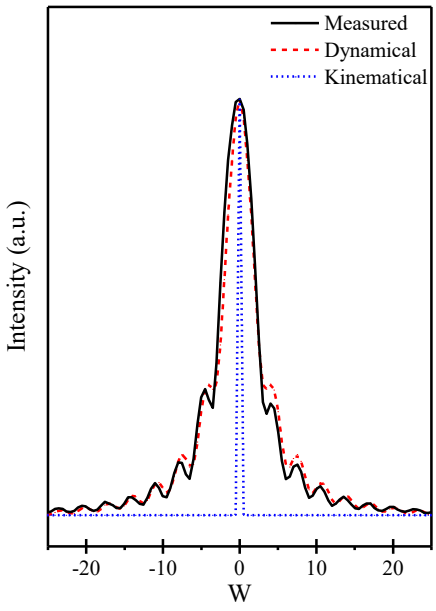

Figure 3.8. Comparison of the measured rocking curve with the theoretical rocking curve by dynamical and kinematical theory for the 011 reflection of the same GI crystals with a thickness of 199 μm, taken with an incident beam with a wavelength of 1.2 Å in BL20B at KEK-PF.

Table 3.1. Comparison of the FWHMs of rocking curves of GI crystals with different thicknesses, measured and calculated using kinematical theory.

Crystal thickness [μm]	FWHM [arcsec]	
	Measured	Calculated using kinematical theory
199	6.98	0.12
260	5.72	0.09
362	5.11	0.06
824	4.64	0.03

increases. Figure 3.9 (a) shows the rocking curve profiles of 011 reflections for GI crystals with different thicknesses of 824 μm, 362 μm, 260 μm, and 199 μm. As seen in the digital X-ray topographs in Figure 3.10, it is confirmed that these crystals are also dislocation-free high-quality ones as the GI crystal shown in Figure 3.2. Additionally, from the X-ray topographic images after the rocking curve measurements, it is also confirmed that these crystals suffer no significant damage such as the generation of dislocations due to X-ray exposure for the rocking curve measurements, as for the GI crystal shown in Figures 3.3 and 3.4.

As shown in Figure 3.9 (a), the period of oscillation on the wing of the rocking curve profile appears to decrease with increasing crystal thickness. Actually, the oscillation would be invisible for crystals with a thickness greater than 824 μm. The invisibility of the oscillation is probably attributed to the smaller period of oscillation below the resolution limit due to the angular divergence of the beam. This result is also consistent with that predicted from Eq. (3.6) according to the dynamical theory of

diffraction.

Fitting by Eq. (3.8) was also performed for the rocking curves of GI crystals with different thicknesses shown in Figure 3.9 (a). The fitting curves are shown in Figure 3.9 (b), where the values of r for thicknesses of 824 μm, 362 μm, 260 μm, and 199 μm are 0, 0.02, 0.14, and 0.38, respectively. By comparing Figures 3.9 (a) and (b), it appears that the accuracy of the fitting becomes increasingly poor with increasing crystal thickness. Especially, the deviation between the theoretical and measured curves is large for the largest GI crystal with a thickness of 824 μm. In particular, the calculated line width is much larger than the measured width. This can be ascribed to the effect of absorption by the crystals. Therefore, the theoretical curves were further calculated according to the dynamical theory

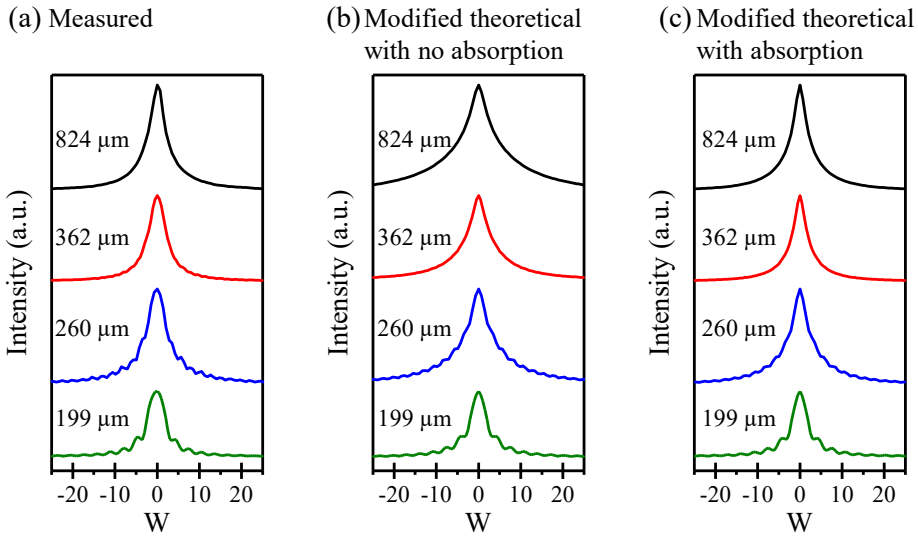

Figure 3.9. Rocking curves for the 011 reflections of GI crystals with different thicknesses of 824 μm, 362 μm, 260 μm, and 199 μm, taken with an incident beam with a wavelength of 1.2 Å in BL20B at KEK-PF. (a) Measured rocking curves, (b) modified theoretical rocking curves with no absorption, and (c) modified theoretical rocking curves with absorption.

with absorption [10] in the symmetric Laue case using the expression

$$\frac{{I_g}^a}{I_o} = \frac{\exp(-\mu H/\cos\theta_B)}{W^2+1}\left\{\sin^2\left(\frac{\pi H\sqrt{W^2+1}}{\Lambda}\right) + \sinh^2\left(\frac{\chi\pi H\sqrt{W^2+1}}{\Lambda}\right)\right\}. \quad (3.9)$$

Note that μ is the linear absorption coefficient, and $\chi = \frac{\chi''}{\chi'}$, where $\chi'$and χ'' are the real and imaginary parts, respectively, of the electric susceptibility. As was done for the fitting of curves with no absorption in Eq. (3.8) mentioned above, the average curve with absorption [10] is added along with a ratio to Eq. (3.9), where the average curve with absorption is given by

$$\frac{{\bar{I}_g}^a}{I_o} = \frac{1}{4(W^2+1)}\left[\exp\left\{\frac{-\mu H}{\cos\theta_B}\left(1-\frac{\varepsilon}{\sqrt{W^2+1}}\right)\right\} + \exp\left\{\frac{-\mu H}{\cos\theta_B}\left(1+\frac{\varepsilon}{\sqrt{W^2+1}}\right)\right\}\right], \quad (3.10)$$

where ε is the dielectric constant.

The calculated curves with absorption are shown in Figure 3.9 (c). The fitting parameters were μ = 0.18 mm^{-1}, χ = 0.001, and ε = 23. The value of the linear absorption coefficient is in good

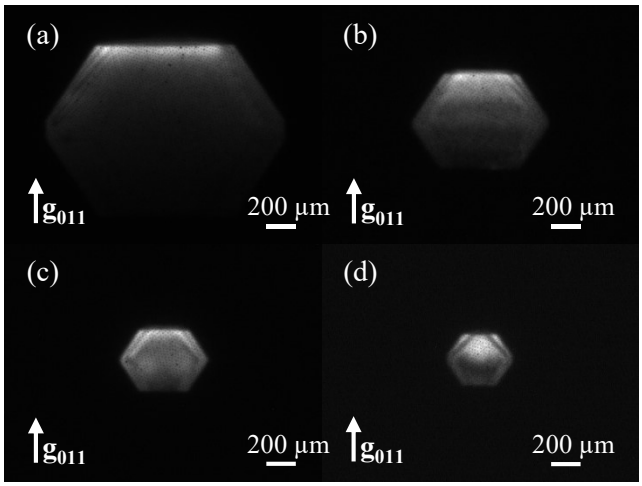

Figure 3.10. Digital X-ray topographs corresponding to the rocking curves shown in Figure 3.9 with different thicknesses of (a) 824 μm, (b) 362 μm, (c) 260 μm, and (d) 199 μm, taken with an incident beam with a wavelength of 1.2 Å in BL20B at KEK-PF. No line contrasts corresponding dislocations are observed in the X-ray topographs, whereas fringe contrasts similar to Pendellösung fringes exhibiting a high crystal quality seem to be observed at the tapered or wedge-like edges of the crystals.

agreement with 0.23 mm^{-1} with λ = 1.2 Å, which is estimated from the mass absorption coefficients and atomic densities of GI crystals containing no intracrystalline water [64]. The slight discrepancy in the values might be attributed to the presence of intracrystalline water in our sample. Additionally, the value of the dielectric constant is also consistent with the typical values of 3–40 for protein crystals, as reported previously [70–72]. On the other hand, the value of χ is of the same order as that estimated from $\chi'\left(=-\frac{Fr_e\lambda^2}{\pi V_c}\right)$ and the imaginary part χ'' and is lower by one order of magnitude than that of hard Si crystals [9]. Therefore, these fitting parameters are reasonable values for protein crystals.

As seen in Figure 3.9 (c), the accuracy of the fitting is largely improved, especially for the largest GI crystals with a thickness of 824 μm. This implies that the rocking curves for the large GI crystals can be also explained by the dynamical theory of diffraction with absorption. Thus, dynamical diffraction occurs for low-order reflections with large structure factors even in protein crystals.

Recently, it was reported that ultrahigh resolution (high-order reflection) crystallographic analysis with high-quality protein crystals and a high-energy beam could provide an accurate structure and charge density of proteins [73]. Especially, the accurate analysis of the electron distribution in proteins becomes increasingly important since the characteristics in proteins are predominantly influenced by valence electrons. Such analysis performed with a high-energy beam can be based on the kinematical theory of diffraction [74]. However, the analysis of the diffraction intensities of low-order reflections

is often poor even when the high-order reflection intensities are well-resolved [75]. The accurate analysis of the diffraction intensities of lower-order reflections is a prerequisite, especially for the evaluation of the valence electron distribution. The analysis of the dynamical diffraction for low-order reflections shown in this work might be useful for obtaining a more accurate structure and charge density of proteins in the future.

Additionally, in protein-crystal-structure analysis and model refinement, there is the basic mystery of why the agreement between the observed and calculated values of the structure factor, F_{obs} and F_{calc} (or between I_{obs} and I_{calc}), is never as good as in the intensity measurements. There are candidate reasons for this of which the need for a dynamical diffraction model or a combined kinematical and dynamical diffraction model is one. The other reasons are the need for the wider adoption of ensemble refinement or more simply the need for the community and the PDB to adopt refereeing of structure articles with the underlying diffraction data. Our results propose the need for a dynamical diffraction model in protein-crystal-structure analysis and model refinement, which has never been used in conventional structural analysis so far.

3.4 Conclusion

We have shown the oscillatory profiles of rocking curves corresponding to low-order reflections with a large structure factor for GI crystals. It was shown that the change in the oscillatory profile with the

wavelength of the incident beam and the thickness of the crystal is well-explained by the dynamical theory of diffraction. From these results, it was concluded that dynamical diffraction similar to that seen in high-quality Si crystals occurs even in protein crystals. This suggests the possibility of the use of dynamical diffraction for the determination of the structure and charge density of proteins.

Chapter 4

Direct observation of stress-induced dislocations in protein crystals by synchrotron X-ray topography

Abstract

Stress-induced dislocations in glucose isomerase (GI) crystals were investigated by synchrotron X-ray topography with simple indentation method. It is observed that the indentation gives rise to the deformation associated with strain and dislocations over the entire crystal. It is characterized that three kinds of mobile dislocations with Burgers vectors of $\frac{1}{2}\langle 111\rangle$, $\langle 100\rangle$ and $\langle 010\rangle$ are at least introduced by the impact stresses due to the indentation. The shapes of the dislocations exhibit half loops and clusters of dislocation loops, as those in common inorganic crystals. It is suggested that the deformation in protein crystals also occurs by the dislocation mechanisms, as those in common inorganic crystals.

4.1 Introduction

Protein crystals are composed of huge protein molecules with complex shapes. The molecular size is an order of nanometer as compared with that of angstrom in common crystals. In addition, they contain a large amount of intra-crystalline water among protein molecules [1,2], in contrast to ordinary crystals.

The behavior of the intra-crystalline water in the crystals is qualitatively classified into two types: one is bound water held around each protein molecules and the other is free water moving through the crystals [77–81]. From such unique characteristics, protein crystals are expected as new materials such as biosensor and bio-porous materials in the next generation [4–6]. Therefore, the knowledge of the mechanical properties of protein crystals is required for practical applications as industrial materials.

In order to understand the mechanical property in crystals, it is important to study the behavior of dislocations [19]. The mechanical property and relationship between dislocations and slip deformation have been studied on many kinds of materials including organic crystals with low molecular weight for a long time [20–25]. However, the mechanical properties of protein crystals have not been fully elucidated yet. Researches on the mechanical property of the protein crystals are limited in numbers. Almost all of them have been carried out on hen egg-white lysozyme (HEWL) crystals with polymorphisms such as tetragonal, orthorhombic, monoclinic and triclinic forms. Micro-Vickers hardness tests with the indentation have been mainly performed on tetragonal and orthorhombic HEWL crystals [55–59]. The hardness is estimated from the size of the plastic deformation, or the indentation mark on the crystal surface. The values of the hardness in fully hydrated condition, or wet condition, are around 16 and 6 ~ 10 MPa for tetragonal and orthorhombic HEWL crystals, respectively [55–59], which are lower than those of common organic and inorganic crystals [82,83]. It is considered that the plastic deformation by the indentation is due to the dislocation mechanism even in protein

crystals. This has been presumed from the observation of slip traces after the indentation [55–59]. The slip deformation associated with the dislocations was also simulated by using a continuum-based crystal plasticity model [84]. The mechanical properties of GI [85], ferritin [86,87], trypsin [86,87], and insulin [86,87] crystals were also investigated by the indentation method and the pushing with the calibrated glass filament. It was found that GI crystals are qualitatively more ductile and less fragile due to the creep phenomenon than HEWL crystals [85]. Such unique mechanical properties can be also related to the characteristics of stress-induced dislocations.

While the mechanical properties of protein crystals have been studied, the dislocations in HEWL crystals have been observed by synchrotron X-ray topography [40,47,48]. The X-ray topography is the only powerful tool for the identification of crystal defects, especially dislocations, in protein crystals, since the protein crystals contain a lot of intra-crystalline water. The characteristics of dislocations depend on the crystal structure in the HEWL crystal where the tetragonal, orthorhombic and monoclinic HEWL crystals have the primitive cell structure of $P4_32_12$, $P2_12_12_1$ and $P2_1$, respectively. In tetragonal and orthorhombic HEWL crystals, it is clearly observed that the straight dislocations are generated around the nucleus center or sector boundary [40,47]. On the other hand, the curve and loop dislocations are observed in monoclinic HEWL crystals [48]. However, almost all of dislocations observed in X-ray topographic experiments so far correspond to so-called grown-in dislocations. To our knowledge, there is no report yet on direct observation of stress-induced

dislocation after the deformation. For comprehensive understanding of dislocations in protein crystals, the research on stress-induced dislocations should be carried out.

According to previous reports [60,61], protein crystals exhibit much low shear modulus compared with other metal, covalent and ionic crystals, although dislocations in protein crystals have large Burger vectors. Therefore, the dislocation self-energy $E \sim \mu b^2$, according to dislocation theory, is relatively low and/or equal to metal crystals, where μ is the shear modulus and b is Burgers vector [19]. This suggests that the dislocations are easily introduced by an applied stress. However, to our knowledge, there is no report yet on direct observation of stress-induced dislocation in protein crystals. This is due to the difficulty of the growth of high quality crystals and the brittleness of protein crystals under the stresses.

Recently, the high quality GI crystals with a body-centered-orthorhombic structure (*I*222) could be grown. They show the clear equal-thickness fringes related to Pendellösung fringes that are an indicator of high quality crystals [49,50]. The grown-in dislocations in GI crystals grown using the cross-linked seed crystals were also observed by synchrotron X-ray topography [50,88]. These dislocations extended from the interface of the seed crystals to the crystal surface. The Burgers vector of the grown-in dislocations was to be the $\langle 111 \rangle$ direction. The clear bead-like contrasts along the dislocation images are also observed in GI crystals [50]. Moreover, when GI crystals are grown with non-cross-linked seed crystals, we can obtain dislocation-free crystals in which the dynamical

diffraction phenomena are observed [89]. The dislocation-free crystals are useful for the observation of the stress-induced dislocations after the deformation.

Even when dislocation-free high-quality protein crystals are obtained, it is difficult to set up the specimens after the deformation for synchrotron X-ray topographic observation. Because the specimens after the deformation are quite brittle and/or fragile. To improve the setup of the samples, we made special specimen holders. The samples mounted in the holders were indented by a needle, and soon observed in-situ by synchrotron X-ray topography. As a result, we succeeded in the observation of dislocations which were induced by the indentation method in dislocation-free GI crystals. In this paper, we report the observation of stress-induced dislocations in the GI crystals by synchrotron X-ray topography.

4.2 Experimental Methods

4.2.1 Crystal growth

The solution of glucose isomerase (GI) from *Streptomyces rubiginosus* was purchased from Hampton Research Corp. and used without further purification. GI crystals were grown by using pure (non chemical cross-linked) seed crystals. The seed crystals were grown from a solution containing 33 mg/mL glucose isomerase, 6 mM tris(hydroxymethyl)-aminomethane (TRIS) hydrochloride (pH 7.0), 0.91 M ammonium sulfate, and 1 mM magnesium sulfate at 20°C via hanging drop technique. After

the seed crystals were grown, the GI crystals were grown on siliconized-cover glasses (Hampton Research Corp.) again from the seed crystals using sitting drop system and the crystallization solution at 20°C for 2 weeks. Finally, the grown crystals on the cover grasses were sealed in acrylic cell (25 mm × 25 mm × 2 mm) and OHP film as shown in Figure 4.1 (c).

The molecular weight of GI is approximately 173,000 and the shape of that is close to spherical. The crystal has a body-centered-orthorhombic structure with space group *I*222, lattice constants of a = 9.39 nm, b = 9.96 nm, and c = 10.29 nm, and two molecules per unit cell [64]. The crystals were bounded by the habit crystallographic faces of $\{110\}$, $\{101\}$, and $\{011\}$ as shown in Figure 4.1 (a) and (b). The molecular arrangements along the a axis, b axis and the unit cell are shown in Figure 4.1 (d), (e) and (f), respectively.

4.2.2 X-ray topography and an indentation

X-ray topography was carried out with synchrotron radiation in BL20B beamline at the Photon Factory (PF) of the High Energy Accelerator Research Organization (KEK). A monochromatic beam of 1.2 Å was selected by adjusting the double-crystal monochromator. The GI crystals sealed in the acrylic cell were mounted on the goniometer using wax. The topographic images by the monochromatic beam were recorded on X-ray films (Agfa D2) with exposure times of about 120 sec before and after an indentation.

The indentation was performed using a sewing needle for a short time within 4 milliseconds by hand. The indentation time was measured by a digital video camera. The needle has an almost hemispherical tip with a curvature radius of around 9 μm. After the OHP film was detached from the acrylic cell, the indentation was carried out. Then, the film was covered on the cell again to prevent evaporation of crystals. The cell with the crystal was put on a stand and the stress was applied on $(0\bar{1}1)$ crystal surface.

4.3 Results and Discussion

In order to introduce dislocations, the indentation was carried out on (011) crystal surface by using a sewing needle within 4 milliseconds by hand. This corresponds to an impact stress. Figures 4.1 and 4.2 show optical micrographs of GI crystal before and after the indentation. As seen in Figure 4.1, as-grown crystal before the indentation exhibits optically high quality containing no cracks. On the other hand, in the crystal after the indentation, the indentation site is clearly observed as *I* indicated by the arrow in Figure 4.2 (b). No cracks are observed in the crystal even after the indentation. It should be noted that some slip traces are appeared to be almost parallel to $[100]$ direction at the edge of the crystal as shown in Figure 4.2 (c). It is considered that the slip traces are related to the dislocation multiplication and motion as reported previously [55–59].

Figure 4.3 shows synchrotron X-ray topographs of GI crystal before and after the indentation,

corresponding to optical micrographs in Figures 4.1 and 4.2. The topographs were taken with 110 reflection. The corresponding schematic figure with the indention site marked *I* is shown in Figure 4.3 (b). The topograph before the indentation in Figure 4.3 (a) exhibits two remarkable features in the as-grown crystal. One is that there are no grown-in dislocations in the crystal. The other is that clear fringe contrasts on the topograph are observed as indicated by an arrow in Figure 4.3 (a). These fringe contrasts are explained by the dynamical diffraction observed in high quality crystals as reported previously [50,89]. These results indicate that the as-grown GI crystal obtained in this experiment is

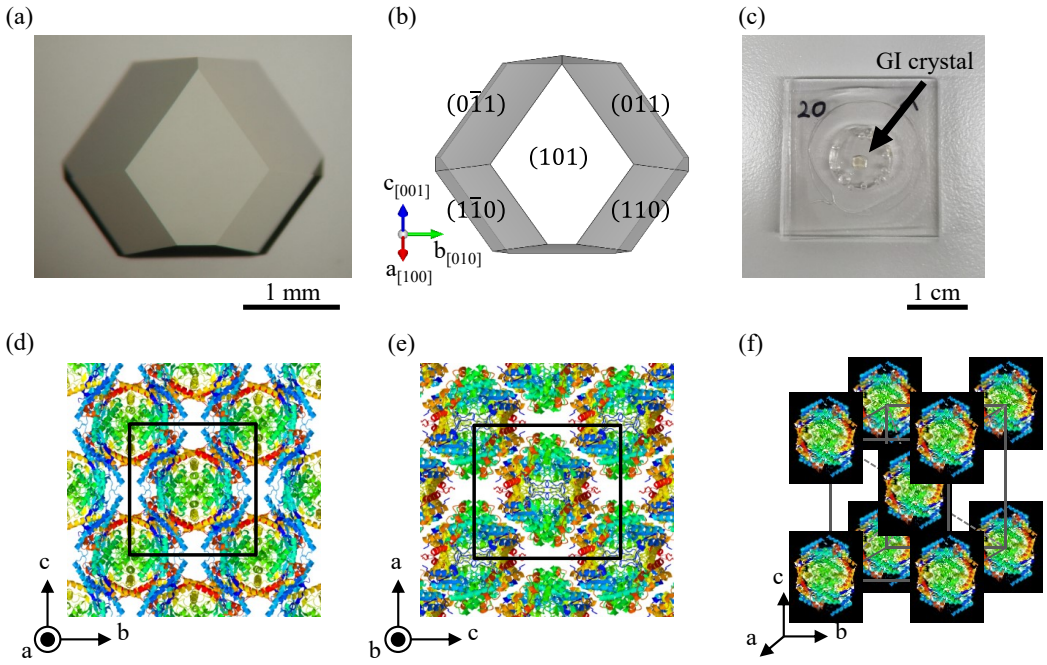

Figure 4.1. Typical GI crystal viewed from the crystallographic direction perpendicular to the (101) plane. (a) Optical micrograph, (b) corresponding schematic prepared with VESTA software [76], (c) GI crystal sealed in an acrylic cell, (d) the molecular arrangements of GI crystals from a view along the *a* axis, (e) the molecular arrangements from a view along the *b* axis, and (f) the unit cell of GI crystals. For easier viewing, the molecular size was changed smaller. Note that there are a lot of water molecules filling between the GI molecules. Schematic of GI molecules were prepared with Jmol software (Jmol: an open-source Java viewer for chemical structures in 3D. http://www.jmol.org/) and Protein Data Bank (ID : 1mnz) [69] for GI crystals.

dislocation-free high-quality crystal. In common protein crystals, grown-in dislocations are always appeared even when the crystals are carefully grown by various growth methods. For example, HEWL crystals contain grown-in dislocation densities of the order of $10^2 \sim 10^3$ cm^{-2} [40,47,48]. Thus, dislocation-free GI crystals used in this experiment have extremely high quality compared with common other protein crystals. The indentation experiments for the observation of stress-induced dislocations were carried out using such high quality GI crystals in this work.

Figure 4.3 (c) shows an X-ray topograph after the indentation for the crystal in Figure 4.3 (a). It should be noted that many kinds of dark contrasts are appeared after the indentation as seen in Figure 4.3 (c). The dark contrasts in the topograph are observed not only near the indentation site but also at the edges of the crystals. On the other hand, the fringe contrasts are still observed at the tapered region of the crystal even after the indentation. This shows that the region without the deformation in the crystal still keeps a high crystal quality.

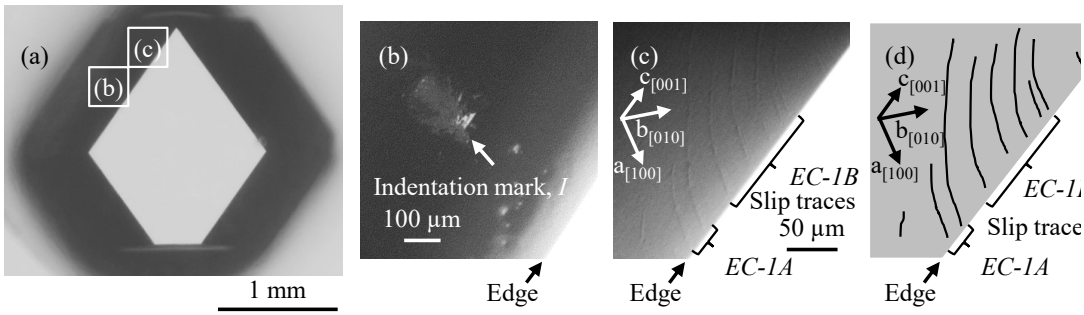

Figure 4.2. (a) Optical micrographs of the GI crystal after the indentation, (b) around the indentation mark, (c) the edge of the crystal, and (d) corresponding schematic. Note that no cracks are observed not only around the indentation but also in overall crystal. The slip traces along [100] direction are clearly observed on $(0\bar{1}1)$ in (c).

To characterize stress-induced dislocations, dark contrasts associated with them are analyzed below. Figure 4.4 shows X-ray topograph after the indentation for the crystal in Figures 4.2 and 4.3 (c), taken with 011 reflection differing from 110 refection in Figure 4.3 (c). As seen in Figure 4.4, the dark contrasts are classified into three kinds of contrasts. First contrasts are appeared at strongly deformed area (*SD*) encircled by solid lines. The contrasts are induced from the indentation site marked *I*, to the crystal edge as shown in Figure 4.4. It seems that the elongated contrasts are composed of cluster of dislocation loops. These contrasts are directly nucleated by the applied stress due to the indentation. Second contrasts exist at weakly deformed area (*WD*) encircled by broken lines. The contrasts at *WD* are separated from the contrasts at *SD* with nodes indicated by white arrows in Figure 4.4. This means that the origin of the dark contrasts at *WD* is different from the dark contrasts at *SD*. Therefore, the contrasts at *SD* and *WD* should be considered separately. The contrasts at *WD* would be indirectly induced by a counter stress (reaction) at the crystal bottom by the indentation at the crystal top, since

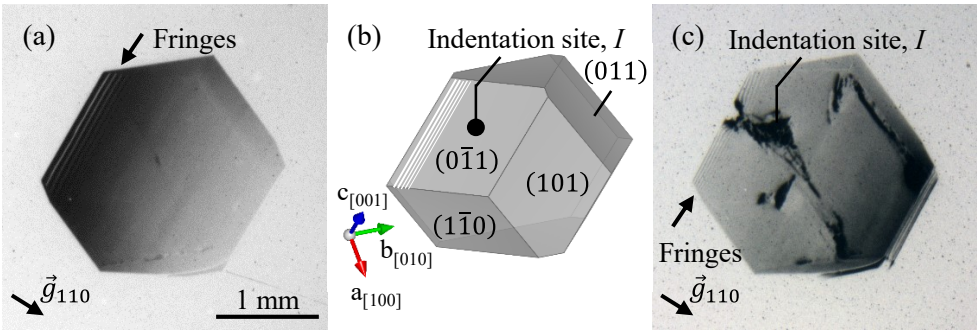

Figure 4.3. (a) Synchrotron monochromatic-beam X-ray topograph of the GI crystal taken with 110 reflection before the indentation. (b) Corresponding schematic which was prepared with VESTA software [76]. (c) The topograph after the indentation in 110 reflection. Note that arrows in (a) and (c) show fringe contrasts similar to Pendellösung fringes. The indentation site is indicated as *I*.

the crystal bottom is contact with a cover glass in the cell. The detail of the setup is shown in Figures 4.6 (d) and (e) later. The third contrasts exist at edges and corners area (*EC*) encircled by dotted lines. Some dark contrasts are appeared at crystal edges and/or corners indicated as *EC-1, EC-2, EC-3, EC-4* and *EC-5* as seen in Figure 4.4. Similar deformation at the edges and corners associated with the indented face has been observed in a tapered Si crystal by TEM observation [90]. According to the report [90], the stress concentration by the indentation occurs not only beneath the indentation but also at the crystal edge and corner on the indented face. Thus it is suggested that similar stress concentration can occur in GI crystals as well. The contrasts at *EC-1*, *EC-4* and *EC-5* correspond to this stress concentration. It seems that other contrasts at *EC-2* and *EC-3* might be accidently introduced during

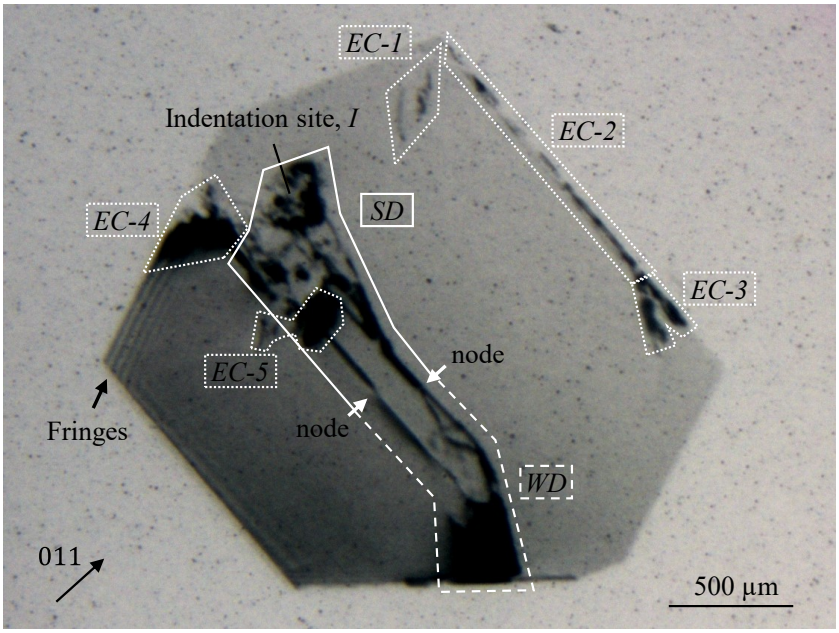

Figure 4.4. Synchrotron monochromatic-beam X-ray topograph of the GI crystal taken with 011 reflection after the indentation. Many kinds of dark contrasts were observed at strongly deformed area (S*D* encircled by solid lines), weakly deformed area (*WD* encircled by dashed lines), and edge and/or corner area (*EC* encircled by dots lines). Note that S*D* and *WD* are separated with nodes indicated by white arrows.

the indentation and/or mishandling.

First let us consider the dark contrasts at *SD* beneath the indentation site as shown in Figure 4.5. The shapes of the dark contrasts around the indentation site *I* are quite complicated and overlapped each other because of the heavy deformation. The line contrast of *SD-1* is visible in 011 and 110 reflections as seen in Figures 4.5 (a) and (c), whereas the contrast at *SD-1* is invisible in $10\bar{1}$ and $0\bar{1}1$ reflections as seen in Figures 4.5 (b) and (d). Such invisibility of the contrasts depending on the reflection indicates that they correspond to dislocations. According to the invisibility criterion for

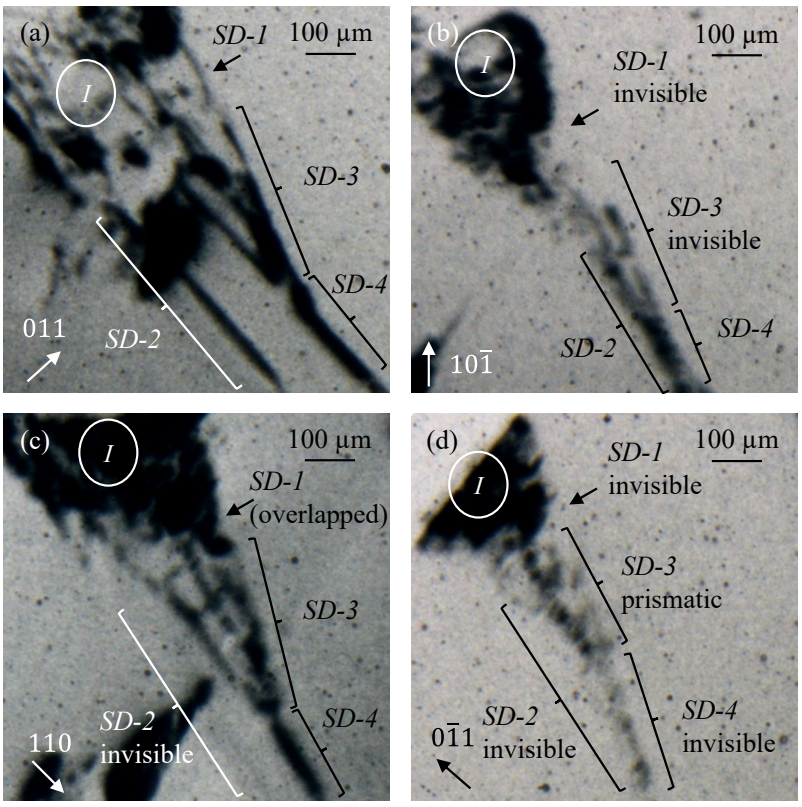

Figure 4.5. Synchrotron monochromatic-beam X-ray topographs taken with (a) 011, (b) $10\bar{1}$ (c) 110 and (d) $0\bar{1}1$ reflections after the indentation, respectively. The contrasts indicated by *SD-1*, *SD-2*, *SD-3* and *SD-4* are invisible in some reflections although the other contrasts are not invisible in all reflections due to the heavy deformation by the indentation. The indentation site is indicated by *I*.

dislocation images ($\boldsymbol{g} \cdot \boldsymbol{b} = 0$; $\boldsymbol{g}$ and $\boldsymbol{b}$ are the diffraction vector and the Burgers vector, respectively), the possible Burgers vector of dislocation of *SD-1* is identified to be $[111]$. The shortest translational vector of $[111]$ in a body-centered-orthorhombic crystal corresponds to a half of the body diagonal. Thus the Burgers vector of the perfect dislocation is assigned to be $\frac{1}{2}[111]$. The group contrasts of *SD-2* are appeared in 011 and 101 reflections as seen in Figures 4.5 (a) and (b). On the other hand, the contrasts at *SD-2* are disappeared with residual contrasts in 110 and $0\bar{1}1$ reflections as seen in Figures 4.5 (c) and (d). According to the invisibility criterion for dislocation images as mentioned above, the possible Burgers vector of dislocation of *SD-2* is identified to be $\frac{1}{2}[1\bar{1}\bar{1}]$. The group contrasts at *SD-3* are appeared in 011, 110 and $0\bar{1}1$ reflections as seen in Figures 4.5 (a), (c) and (d), whereas the contrasts at *SD-3* are disappeared with weak residual contrasts in $10\bar{1}$ reflection as seen in Figure 4.5 (b). According to the invisibility criterion for dislocation images, the possible Burgers vector of dislocation of *SD-3* is identified to be $[010]$. Similarly, the contrast at *SD-4* is disappeared with weak residual contrasts in $0\bar{1}1$ reflection as seen in Figure 4.5 (d). The invisibility criterion for dislocation images shows that the possible Burgers vector of dislocation of *SD-4* is identified to be $[100]$. In addition, it seems that the shapes of the contrasts (*SD-2*, *3* and *4*) around the indentation site *I*, are composed of aligned dislocation loops as shown in Figures 4.5 (b), (c) and (d) although the contrasts and shapes slightly change with reflections. Thus, these dislocation loops are similar to those of prismatic dislocation loops in AgCl crystals which are introduced by an

impact stress using a glass sphere [91]. According to the surface indentations, prismatic dislocation loops are introduced when an indenter strongly enough presses on the surface of a crystal [92]. Therefore, even in GI crystals, the dislocation loops are introduced by the indentation with the impact stress.

Next let us consider the line contrasts of *WD-1* and *WD-2* at *WD* as shown in Figures 4.6 (a), (b) and (c). It seems that the line contrasts of *WD-1* and *WD-2* are elongated from the dark contrast of *WD-3* as seen with 011 reflection in Figure 4.6 (a). The line contrasts of *WD-1* and *WD-2* are disappeared in 110 and $0\bar{1}1$ reflections with residual contrasts as seen in Figure 4.6 (b) and (c). Note that the elongated contrasts of *WD-1* and *WD-2* appear to be visible in $0\bar{1}1$ reflection as seen in Figure 4.6 (c) since their residual contrasts are overlapped each other in the reflection setup. Thus, the invisibility of the contrasts with the reflection also shows that the line contrasts of *WD-1* and *WD-2* correspond to dislocations. According to the invisibility criterion for dislocation images, the Burgers vectors is identified to be $\frac{1}{2}[1\bar{1}\bar{1}]$. On the other hand, the dark contrast of *WD-3* is appeared in various reflections. This means that the origin of the dark contrast of *WD-3* is different from those of *WD-1* and *WD-2*. So we suggest a model of dislocation mechanisms for *WD*. The dislocations of *WD-1* and *WD-2* are elongated from the dark contrast of *WD-3* as mentioned above. This shows that the dislocations of *WD-1* and *WD-2* are introduced by a stress concentration at the crystal bottom. This stress corresponds to the counter stress at the crystal bottom due to the indentation at crystal top, since

the crystal bottom is contact with the cover glass in the cell as shown in Figures 4.6 (d) and (e). To elucidate the detail of the mechanism, further analysis with simulation models on crystal contact is needed.

Finally, let us consider the line contrasts of *EC-1A*, *EC-1B* and *EC-2A* at *EC-1* and *EC-2* as shown

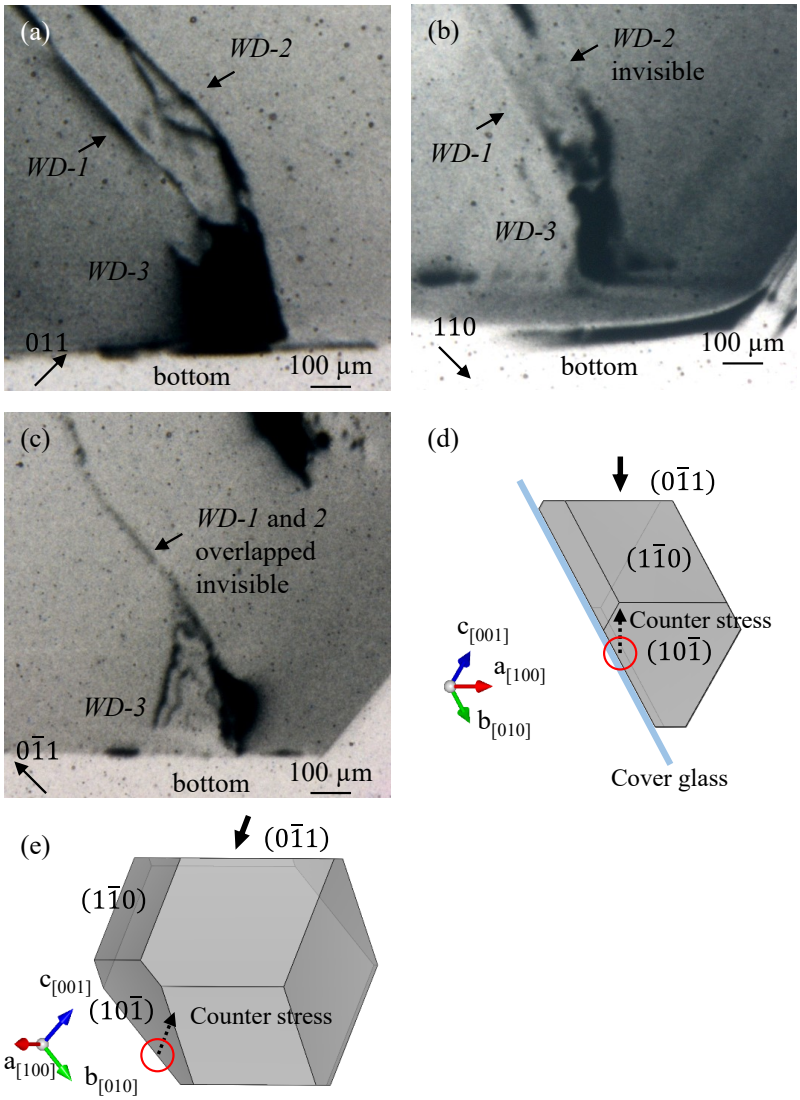

Figure 4.6. Synchrotron monochromatic-beam X-ray topographs of the GI crystal taken with (a) 011, (b) 110 and (c) 0$\bar{1}$1 reflections after the indentation, respectively. (d, e) Schematics of the distribution of the indentation force. The counter stress would be occurred at the contact area between the crystal bottom and cover glass (red circle area). The schematics were prepared with VESTA software [76].

in Figures 4.7 (a) and (b). As shown in Figure 4.7 (a), all contrasts of *EC-1A*, *EC-1B* and *EC-2A* are visible in 020 reflection. The contrasts are also visible in other 110 and 011 reflections. On the other hand, they are disappeared in 101 reflection. This invisibility of the contrasts depending on the reflection indicates that the line contrasts correspond to dislocations. According to the invisibility criterion for dislocation images, it is identified that the dislocations of *EC-1A*, *EC-1B* and *EC-2A* have the Burgers vector of $[010]$. Especially, the direction of the line contrasts related to dislocations of *EC-1A* and *EC-1B* is in good agreement with the slip traces with $[100]$ direction as shown in Figure 4.2 (c). Thus it is obvious that the line contrasts correspond to slip dislocations. The lengths of the line contrasts of *EC-1A* and *EC-1B* are measured to be 340 and 330 μm, respectively, as seen in Figure 4.7 (a). On the other hand, the lengths of the slip traces corresponding to *EC-1A* and *EC-1B* are measured to be 190 and 150 μm, respectively, as seen in Figure 4.2 (c). The difference of the length is attributed to the underestimation of the slip traces. From the Weiss' law of zones, possible slip planes with $[100]$ slip traces are (010), (001), (011) and $(0\bar{1}1)$. However, (010), (011) and $(0\bar{1}1)$ are not suitable as the slip plane since the Burgers vector of $[010]$ identified above is not to be on them. As a result, (001) is assigned as possible slip plane. Thus, the slip system corresponding to the slip dislocations at *EC-1A*, *EC-1B* and *EC-2A* is identified to be $(001)[010]$. The schematic figures of the slip system and dislocations are shown in Figures 4.7 (c) and (d). The dislocation lines would be

composed of dislocation half-loops which are emitted from a dislocation source as seen in Figures 4.7 (c) and (d), although it is difficult to resolve the loop shapes by common synchrotron X-ray topography. For other dark contrasts at *EC-3, EC-4* and *EC-5* in Figure 4, the features such as Burgers vectors of dislocations could not be characterized in this work.

In this research, it is clarified that the deformation of GI crystals is controlled by nucleation and multiplication of dislocations. The observation by synchrotron X-ray topography clearly shows that the stress-induced dislocations were nucleated from dislocation-free GI crystals after the indentation.

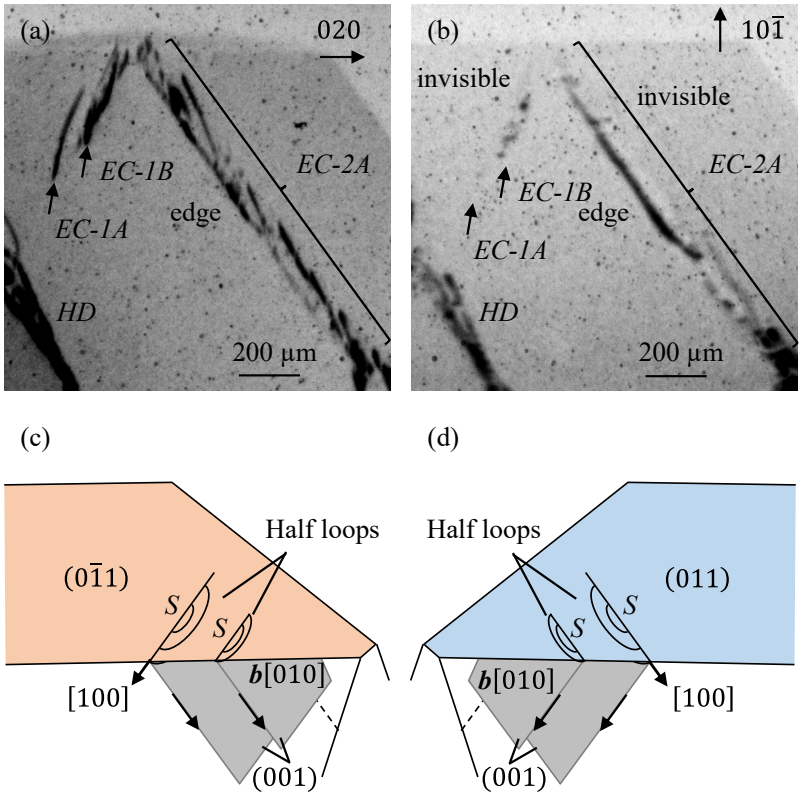

Figure 4.7. Synchrotron monochromatic-beam X-ray topographs of the GI crystal taken with (a) 020 and (b) 10$\bar{1}$ reflections after the indentation, respectively. The contrasts indicated by *EC-1A*, *EC-1B* and *EC-2A* are invisible with weak residual contrasts. (c, d). Schematic figures of the habit planes and dislocation motion with slip deformation. A dislocation source is indicated by *S*.

Moreover, the stress-induced dislocations in GI crystals have some kinds of the Burgers vectors such as $\frac{1}{2}[111]$, $\frac{1}{2}[1\bar{1}\bar{1}]$, $[100]$ and $[010]$ as shown in Table 4.1. In general, dislocations with shorter length of the Burgers vectors are easily introduced [19]. As shown in Table 4.2, there is little significant difference in the length of the Burgers vectors in GI crystals. Therefore, the dislocations with different Burgers vectors can be introduced in GI crystals. Actually, in previous report [58], the deformation of orthorhombic HEWL crystals has been occurred by slip deformation with six kinds of slip systems. Thus, it is considered that the dislocations with some kinds of the Burgers vectors are introduced in protein crystals.

Protein crystals contain a large amount of intra-crystalline water in contrast to common crystals. Moreover, they are composed of protein molecules with the huge and complex shape. In spite of such unique features in protein crystals in contrast of common inorganic crystals, it is concluded that the deformation due to the dislocation mechanisms occurs not only in inorganic crystals but also in protein crystals.

Table 4.1. The observed Burgers vectors of dislocations in GI crystals.

Area	Dislocations	Burgers vector $\boldsymbol{b}$
SD (Strongly deformed)	*SD-1*	$\frac{1}{2}[111]$
	SD-2	$\frac{1}{2}[1\bar{1}\bar{1}]$
	SD-3	$[010]$
	SD-4	$[100]$
	except *SD-1, 2, 3* and *4*	unknown
WD (Weakly deformed)	*WD-1*	$\frac{1}{2}[1\bar{1}\bar{1}]$
	WD-2	$\frac{1}{2}[1\bar{1}\bar{1}]$
	WD-3	unknown
EC (Edges and corners)	*EC-1A*	$[010]$
	EC-1B	$[010]$
	EC-2	$[010]$
	EC-3	unknown
	EC-4	unknown
	EC-5	unknown

Note that the all dislocations are shown in Figure 4.4–4.7.

Table 4.2. The possible Burgers vectors in GI crystals.

Burgers vector $\boldsymbol{b}$	$\lvert\boldsymbol{b}\rvert$ [nm]
$[100]$	9.39
$[010]$	9.96
$[001]$	10.29
$[101]$	13.93
$[011]$	14.32
$[110]$	13.69
$\frac{1}{2}[111]$	8.56

4.4 Conclusions

We have shown the dislocation behaviors in glucose isomerase crystals of one of protein crystal investigated by a simple indentation method and synchrotron X-ray topography. The dislocations introduced under the impact stress by the indentation were composed of dislocation loops with different Burgers vectors of $\frac{1}{2}\langle 111\rangle$, $\langle 100\rangle$ and $\langle 010\rangle$, respectively. It is clear that the deformation due to the dislocation mechanisms occurs not only in inorganic crystals but also in protein crystals although they are composed of protein molecules with the huge and complexed shapes.

Chapter 5

General discussion and conclusion

First of all, the author would like to insist that the growth of large high-quality of protein crystals with large-size is the breakthrough in this work. In this thesis, it is shown that dynamical diffraction of X-ray has been occurred even in protein crystals such as glucose isomerase crystals. This indicates that it is possible to obtain the perfect crystals of proteins. Using the extremely high-quality protein crystals, the intrinsic mechanical properties such as dislocations behavior are elucidated by X-ray topography and the indentation method. Thus, it is expected to evaluate the intrinsic physical properties such as not only mechanical properties but also thermal, electrical, magnetic and optical properties.

The crystal perfection of protein crystals such as glucose isomerase crystals was investigated by rocking curve measurement using synchrotron monochromatic-beam X-ray topography. As seen in Figures 3.7 and 3.9, the oscillatory profile of rocking curve was clearly observed. The change in the oscillatory profile with the wavelength of the incident beam and the thickness of the crystal is in good agreement with that predicted using the dynamical theory of X-ray diffraction. It is demonstrated that dynamical diffraction similar to that seen in high-quality Si crystals occurs even in protein crystals.

Some researches of the rocking curve measurement have been carried out so far. However, there is no report of the oscillatory rocking curves by dynamical diffraction in protein crystals. Based on this study, it is considered that there are mainly two factors for observation of dynamical diffraction such

as the oscillatory rocking curves. One is, above of all, the crystal perfection of protein crystals. In order to give the multiple scattering of X-ray in crystals, the crystal perfection must need to be perfect. If there are some defects in crystals, the predominant tendency of the X-ray diffraction is not dynamical diffraction but kinematical diffraction. In pioneer researches on X-ray topographic measurement of HEWL crystals, a lot of crystal defects, *e.g.* dislocations, have been characterized. In the case of GI crystals, however, it is possible to obtain the perfect crystals.

Here, let us consider the different properties between HEWL and GI molecules. As shown in Figure 5.1(a), HEWL molecules exist as monomer in a stable state. The molecular shape is not spherical but spheroid like a Croissant. The molecular weight of HEWL is approximately 13,000. On the other hand, GI molecules exist as tetramer in a stable state. The molecular weight of GI as tetramer is approximately 173,000. As shown in Figure 5.1(c), the molecular shape is almost spherical although the monomer (a part of tetramer as seen in Figure 5.1(b)) is asymmetric one as HEWL molecules. Moreover, GI crystal has a body-centered-orthorhombic structure with space group *I*222, lattice

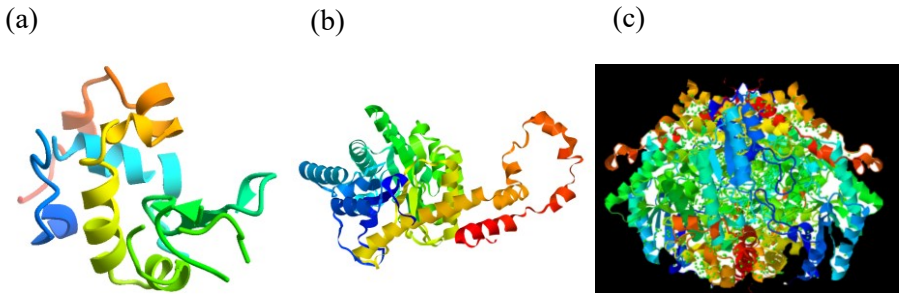

Figure 5.1. (a) A hen egg-white lysozyme molecule, (b) monomer of glucose isomerase molecule, and (c) tetramer of glucose isomerase molecule. Note that the stable state of glucose isomerase is tetramer form.

constants of a = 9.39 nm, b = 9.96 nm, and c = 10.29 nm, and two molecules per unit cell. The ratio of the lattice parameters, a : b : c, is 1.00 : 1.06 : 1.10, respectively. The ratio has almost 1.0. It looks like body-centered cubic (BCC) structure. The simple shape of the molecule and simple structure of the crystal might contribute the crystal perfection even if the crystals are composed of protein molecules. To elucidate the factors for perfect crystals of proteins, further investigations such as using other proteins are desired.

In general, the radiation damage by X-ray irradiation often occurs for protein molecules [51,65,66,98–100]. To form the perfect crystals, the perfection of the protein molecules own is also important. In the case of structural analysis, the undetected atoms due to the breakage of the protein molecules are allowed to reach large Debye-Waller temperature factor, *i.e.* B-factors [101]. As a result, the resolution of the structural analysis becomes poor. However, in the case of X-ray topography, the diffraction is originated from the average intensity by the scattering power of the volume. The effective pixel size of the CCD camera corresponding to the spatial resolution in this study is 6.45×6.45 μm^2. Even if a few GI molecules have been broken by the radiation damage, it is difficult to identify the effect of the molecules. Therefore, in the scale of X-ray topographic measurement, they have little effect on the perfection of crystals. In order to elucidate the effect of the broken molecules, measurement with nanoscale such as using cryo-EM would be needed.

The other factor for observation of dynamical diffraction is the angular resolution of the X-ray optics

evaluated by DuMond diagram [67] (described at Appendix B in this thesis). From Eq. 3.3 ($\omega = \frac{2}{\pi}\frac{r_e}{V_c}\frac{|F|\lambda^2}{\sin 2\theta_B}$), the value of full width at half maximum (FWHM), ω, is proportional to $|F|/V_c$, where $|F|$ is the magnitude of the structure factor and V_c is the volume of the unit cell. In the case of protein crystals, the value of FWHM for the rocking curve is narrower than those of inorganic materials due to the large unit cell and relatively small magnitude of the structure factor. If the value of the angular resolution of the X-ray optics is larger than that of FWHM, it is difficult to resolve the intrinsic rocking curve profiles for protein crystals. The angular resolution of the X-ray optics is important to identify the intrinsic rocking curves for protein crystals. As mentioned at section 3.3.3 in Chapter 3, the angular resolution of the optics for the 011 reflection of GI crystals was evaluated to be 7.06×10^{-4}° at BL-20B in KEK-PF. A value of the intrinsic FWHM of the rocking curves for the 011 reflection for GI crystals was also estimated as 1.32×10^{-3}° in the experimental condition. This value was larger than that of the angular resolution of the optics at BL-20B in KEK-PF. Therefore, it is possible to resolve the intrinsic rocking curves of GI crystals. On the other hand, the value of the intrinsic FWHM of the rocking curves for the 440 reflection of tetragonal HEWL crystals, which are mainly used as model reflection and protein crystals for a lot of investigations, was also calculated as 1.17×10^{-4}° in the same experimental condition. A value of the angular resolution of the optics for 440 reflection of tetragonal HEWL crystal is also evaluated to be 7.80×10^{-4}°. The value of intrinsic FWHM of tetragonal HEWL crystals is smaller than that of the angular resolution of the optics. This indicates that even if the perfect

crystals of tetragonal HEWL are obtained, it is difficult to observe the intrinsic rocking curves of the crystals. The values of the intrinsic FWHM for the rocking curves of GI and tetragonal HEWL crystals and the angular resolution of the optics are summarized in Table 5.1. The correlation between the angular resolution of the X-ray optics and the value of the intrinsic FWHM for the rocking curves is important key to measure the intrinsic behavior of the rocking curves. Therefore, in order to understand the behavior of dynamical diffraction in protein crystals, it is much important not only to grow perfect crystals of proteins but also to comprehend the angular resolution of the X-ray optics. Why the pioneer researches on the rocking curve measurements of protein crystals, mainly HEWL crystals, could not observe dynamical diffraction? It might be due to the poor angular resolution of the X-ray optics although they may have been succeeded to grow the perfect crystals of proteins. Owing to the development of the synchrotron radiation, the performance of the X-ray optics has been improved so far. SPring-8, which is one of the synchrotron facilities, has been used as next generation synchrotron compared with KEK-PF. In the case of the X-ray optics at BL38B1 in SPring-8 (where the comparison of the facility status are summarized in Table 5.2), the value of the angular resolution for 440 reflection of tetragonal HEWL crystals is estimated as 2.67×10^{-4}°. This value is almost comparable to that of the intrinsic FWHM for 440 reflection of tetragonal HEWL crystals. If it has been already succeeded to grow the perfect crystals of tetragonal HEWL, it might be possible to observe the oscillatory rocking curves using BL38B1 in SPring-8. As a future work, the observation of dynamical diffraction in

Table 5.1 Comparison of the intrinsic FWHM and angular resolution for GI and tetragonal HEWL crystals.

Crystal	Reflection	Structure Factor $\|F\|$	FWHM [$\times 10^{-3o}$]	Angular resolution [$\times 10^{-3o}$]	
				KEK-PF BL20B	SPring-8 BL38B1
GI	0 1 1	14,380	1.32	0.71	0.08
Tetragonal HEWL	4 4 0	1,611	0.12	0.78	0.27

Note that the incident wave length λ is 1.2 Å.

Table 5.2 Comparison of the facility status for KEK-PF BL20B and SPring-8 BL38B1.

Facility	σ_y [μm]	$\sigma_{y'}$ [μrad]	L [m]	$\Delta\theta$ [$\times 10^{-3o}$]
KEK-PF BL20B	59	12	14.35	12.5
SPring-8 BL38B1	11.6	0.5	50	3.47

σ_y: vertical beam size, $\sigma_{y'}$: vertical beam divergence, L: distance between the light source and the X-ray detector, $\Delta\theta$: beam divergence estimated from the geometry of the experimental system.

HEWL crystals are expected using high performance synchrotron source. In addition, the measurements of various protein crystals except GI and HEWL crystals are desired for elucidation of the perfection of protein crystals.

The observation of dynamical diffraction in protein crystals suggests as follows; one is the need for a dynamical diffraction model in protein-crystal structure analysis and model refinement analysis. It has never been used in conventional structural analysis. The other is the possibilities of elucidation the intrinsic physical properties such as mechanical, thermal, electrical, magnetic and optical properties of protein crystals. It has been difficult to understand the behavior of protein crystals since the crystal quality has been poor so far.

As the first step, the mechanical properties were elucidated using perfect crystals of proteins by simple indentation method and synchrotron monochromatic-beam X-ray topography. As seen in Figure 4.3, the stress-induced dislocations in protein crystals were clearly observed by X-ray topography. They were identified as three types of dislocations with different Burgers vectors at least.

For ordinary materials such as inorganic crystals, the deformation is controlled by the dislocation nucleation and motion. On the other hand, in the case of protein crystals, although pioneer studies have suggested the existence of stress-induced dislocations, none of them has provided direct observation of the dislocations due to the difficulty of the growth of high-quality crystals and the brittleness of protein crystals. This study is unique in terms of demonstrating the first observation of stress-induced dislocations in protein crystals with high crystal perfection. These observations demonstrate that the deformation in protein crystals by the indentation occurs due to the dislocation mechanisms, as those in inorganic crystals. However, casting an eye on the detailed behavior, there are some discrepancies.

As mentioned above, GI crystal has a pseudo-BCC structure. A comparison of the arrangements of GI molecules and Fe atoms is shown in Figure 5.2. In general, the Burgers vector of dislocations and its slip plane in crystals such as Fe with BCC structure are $\langle 111 \rangle$ and $\{110\}$, respectively [19]. However, the Burgers vectors are $\frac{1}{2}[111]$, $\frac{1}{2}[1\bar{1}\bar{1}]$, $[100]$ and $[010]$ in GI crystals with the pseudo-BCC structure. The Burgers vectors of $[100]$ and $[010]$ are different from those of BCC materials. Moreover, the slip plane of the dislocations with the Burgers vector of $[010]$ is (001).

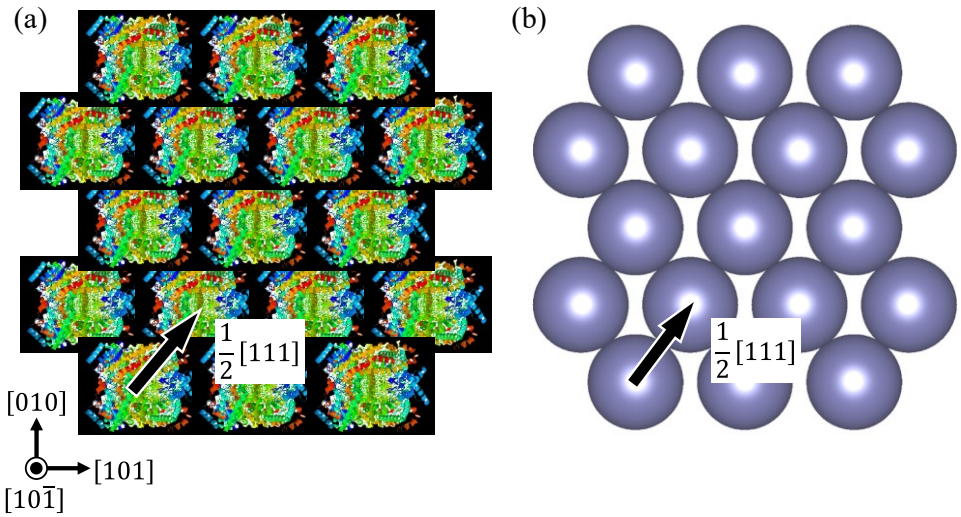

Figure 5.2. Comparison of the arrangements of (a) GI molecules and (b) Fe atoms.

This slip system is unique compared with that of BCC materials. Thus, it implies that the dislocations with some kinds of the Burgers vectors are introduced in protein crystals.

For pioneer researches on the mechanical properties of protein crystals, the observation of the dislocation behavior have not been succeeded due to the poor-quality protein crystals containing crystal defects. Using perfect crystals of proteins, however, it is possible to demonstrate careful observation and characterization of the mechanical properties of protein crystals. As more advanced investigations, the measurement of dislocation behavior such as glide velocities of dislocations in protein crystals is of interest from the view point of materials science. It can be speculated that the glide velocities are different from those of inorganic materials since the magnitude of Burgers vectors in protein crystals is much larger. These features might be expected to give rise to unique mechanical properties for the practical applications. Using the high-quality protein crystals, it must be possible

not only to elucidate the fundamental physical properties but also to apply the protein crystals for novel materials such as protein hybrid devices.

Finally, as the future works, it is expected that a new evaluation method of crystals is developed using dynamical diffraction. Dynamical diffraction is quite sensitive for the crystallinity and crystal defects. Recently, characteristic images are observed by X-ray topographic measurement. As shown in Figure 5.3(a), unique contrasts like insects or centipede are clearly observed. This crystal was irradiated by the focused X-ray beam which is conventional one for structural analysis of protein molecules. It seems that the contrasts have a periodic structure as shown in Figure 5.3(b). When the crystal has a few defects (the area except for defects is perfect), the scattering X-ray gives unique contrasts, where they arise from the interference between the new wave field created below the defect and the undeviated original wave field propagating in the perfect regions of the crystal [10]. As mentioned above, in general, the radiation damage by X-ray irradiation is serious problem for

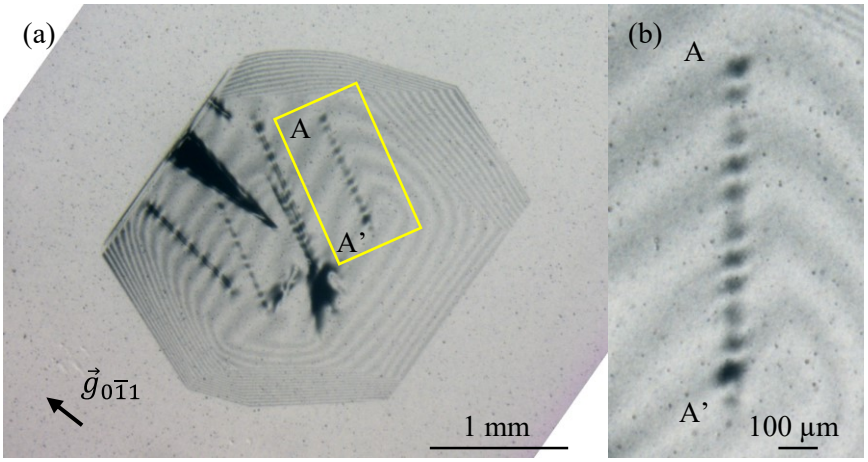

Figure 5.3. (a) X-ray topographic image of the GI crystal irradiated by the conventional X-ray beam for structural analysis, (b) the enlarged image of the yellow rectangular area in (a).

structural analysis of protein molecules. However, there is no report of elucidation of the radiation damage in terms of topological view such as crystal defects in protein crystals. Using perfect crystals of proteins and X-ray topographic measurement associated with dynamical diffraction, crystal defects such as dislocations and radiation damages will be characterized more precisely.

We have made the assessment of the perfection of protein crystals such as glucose isomerase crystals by synchrotron monochromatic-beam X-ray topography, and then we have carried out the elucidation of the mechanical properties using extremely high-quality protein crystals. The results in this work are summarized as follows;

Chapter 3

- The oscillatory profiles of rocking curves for glucose isomerase crystals have been clearly observed. The change in the oscillatory profile with the wavelength of the incident X-ray beam and the thickness of the crystal is well explained by the dynamical theory of X-ray diffraction.
- It was found that dynamical diffraction similar to that seen in high-quality Si crystals occurs even in protein crystals.
- It is expected that perfect crystals of proteins make it possible not only to use the dynamical diffraction for the determination of the structure and charge density of proteins, but also to elucidate the intrinsic physical properties of protein crystals for the practical applications.

Chapter 4

- The dislocation behaviors in high-quality glucose isomerase crystals has been investigated by the indentation method and synchrotron monochromatic-beam X-ray topography.
- The dislocations introduced under the impact stress by the indentation were composed of dislocation loops with different Burgers vectors.
- It is clear that the deformation due to the dislocation mechanisms occurs not only in inorganic crystals but also in protein crystals although they are composed of protein molecules with the huge and complex shapes.

Appendix A (Reference Reports):

Characterization of grown-in dislocations in high-quality glucose isomerase crystals by synchrotron monochromatic-beam X-ray topography

Abstract

High quality glucose isomerase (GI) single crystals are grown by using chemical cross-linked seed crystals. The crystal structure is an orthorhombic system in which the molecular arrangement is close to a body-centered cubic (bcc) one. The crystal defects, especially dislocations, in GI crystals are experimentally characterized by synchrotron monochromatic-beam X-ray topography. Two straight dislocations are clearly observed, which originate from the interface between the cross-linked seed crystal and the grown crystal. From the invisibility criterion of the dislocation images, it is experimentally identified that they are close to be of pure edge character with the Burgers vector of $[1\bar{1}1]$ which is typical one in bcc metal crystals. Moreover, bead-like contrasts along the dislocation images and the equal-thickness fringes, related to Pendellösung fringes, at crystal edges are clearly observed, which have never been observed in other protein crystals so far. These contrasts can attributed to the dynamical diffraction effect which has been often observed in high-quality crystals such as Si. Thus, the perfection of GI crystals is extremely high compared with other protein crystals.

A.1. Introduction

The characterization of crystal defects in protein crystals is important for the growth of high-quality crystals and the understanding of physical properties. X-ray topography is one of the most powerful methods for the mapping and identification of crystal defects, especially dislocations, in crystals [10,26–28]. Since 1996, many groups have carried out the studies on crystals defects in protein crystals, mainly hen egg-white lysozyme (HEWL) crystals, by using synchrotron radiation X-ray topography [29–44]. However, the topographic contrasts of crystal defects from protein crystals are poor compared to those seen for common inorganic crystals and organic crystals of small molecule. The poor contrasts can be attributed to not only the poor crystal quality but also the submillimeter crystal size which is smaller than the lower limit of crystal thickness of typical protein crystals for kinematic contrasts, i.e. direct images, in X-ray topography [26,28,45].

We have obtained relatively clear topographic contrasts for millimeter-size HEWL crystals by using synchrotron monochromatic-beam X-ray topography [44–46]. Furthermore, recently, we succeeded in the growth of glucose isomerase (GI) crystals with large size and high quality for next microgravity experiments [88]. The topographic contrasts of crystal defects, especially dislocations, were much clear compared with those in almost previous papers regarding protein crystals. Such GI crystals are useful for detailed analysis of topographic contrasts from protein crystals by X-ray topography. We

suggested a Burgers vector of dislocations in GI crystals in the previous paper [88]. However, the characterization of dislocations is experimentally insufficient. In this paper, we report experimental identification of dislocations such as its direction and Burgers vector in high-quality GI crystals by synchrotron monochromatic-beam X-ray topography. Note that chemically cross-linked seed crystals are used for the growth of GI crystals including a few dislocations as previous report [88]. Additionally it should be noted that bead-like contrasts along dislocation images and equal-thickness fringes, related to Pendellösung fringes, at crystal edges are clearly observed in GI crystals, which have never been seen in other protein crystals so far.

A.2. Experimental Methods

A.2.1 Crystal growth

Glucose isomerase (GI) was purchased from Hampton Research. The details of the quality o f GI sample is described in https://hamptonresearch.com/documents/product/0000000056-00000 00427.html. The GI sample was used without further purification after filtering with pore siz e of 0.1 μm. Large GI crystals were grown by using seed crystals chemically cross-linked b y glutaraldehyde according to below procedure. First the seed crystals were grown from a cr ystallization solution containing 33 mg/mL glucose isomerase, 6 mM tris(hydroxymethyl)-ami nomethane (TRIS) hydrochloride (pH 7.0), 0.91 M ammonium sulfate, and 1 mM magnesiu

m sulfate by hanging drop technique. For the cross-linking, the seed crystals were immersed into 2.5 wt% glutaraldehyde with 0.91 M ammonium sulfate for 20 min at room temperatur e. The seed crystals cross-linked by glutaraldehyde were rinsed in 0.91 M ammonium sulfate solution to remove residual one on crystal surface. After that, a cross-linked seed crystal w as put in a crystallization droplet on a siliconized cover glass where the droplet is the same solution as that for the growth of the seed crystals as mentioned above. To avoid the heter ogeneous nucleation, the droplet containing the cross-linked seed crystal was annealed at 40° C for 30 minutes. After the annealing, GI crystals were grown from the cross-linked seed cr ystals by sitting drop system. The amounts of the drop solution and reservoir solution are 2 0 μL and 1 mL, respectively. The droplet containing the cross-linked seed crystal was kept at 20°C for 2 weeks so that millimeter-size crystals were obtained.

The crystals were body center orthorhombic with space group *I*222, lattice constants of a = 9.39 nm, b = 9.96 nm, and c = 10.29 nm, and two molecules per unit cell [64]. The crystals were bounded by the habit planes of $\{110\}$, $\{101\}$, and $\{011\}$ as shown in Fig. A.1(b).

A.2.2 X-ray topography

For X-ray topography, the obtained GI crystal with droplet on the cover glass was transferred into an acrylic cell (20 mm×20 mm×2 mm) with a hole (φ=10 mm). The GI crystal was sealed in the cell coved with a polyester film after the solution around the crystal was removed. The cell containing the

GI crystal was mounted on the goniometer. The alignment of optical axis was performed using a microscope.

X-ray topography was carried out with synchrotron radiation in BL20B beamline at the Photon Factory (PF) of the High Energy Accelerator Research Organization (KEK). A monochromatic beam of 1.2 Å was selected by adjusting the double-crystal monochromator. An X-two-dimensional digital CCD camera (Photonic Science X-RAY FDI 1.00:1) was employed to find the target reflections for the X-ray topography. The camera length was 20 cm. The topographic images by the monochromatic beam were recorded on X-ray films (Agfa D2) with exposure times of about 180 sec.

A.3. Results and Discussion

Fig. A.1 shows an optical micrograph of a typical GI crystal and the corresponding schematic figure. The central part with yellow color of the crystal, indicated by an arrow, corresponds to the cross-linked seed crystal, since the yellow color originates from the cross-linking solution with glutaraldehyde. Using this crystal, X-ray topographs were taken in various reflections as shown in Figs. A.2 and A.3.

Fig. A.2(a) shows typical X-ray topograph of the GI crystal, taken with $1\bar{1}0$ reflection. The orientation of the crystal in the topographic experiment corresponding to Fig. A.2(a) is schematically shown in Fig. A.2(b), where the outline of the crystal containing dislocation lines is drawn by using a VESTA software [76]. The incident X-ray beam is in a direction almost vertical to the surface of paper

in Fig. A.2(b). Therefore, the topograph in Fig. A.2(a) corresponds to the projection of the crystal to the surface of paper in Fig. A.2(b). As seen in Fig. A.2(a), the topographic contrasts are much clear, compared with those in other protein crystals such as lysozyme crystals reported so far [29–44,46–48]. This is attributed to the high quality.

First we consider two kinds of main dark contrasts: one is circle-like contrasts at the central part of the crystal and the other is two straight line contrasts elongated from the central part. These dark contrasts correspond to the strain and crystal defects associated with the local misorientation of lattice.

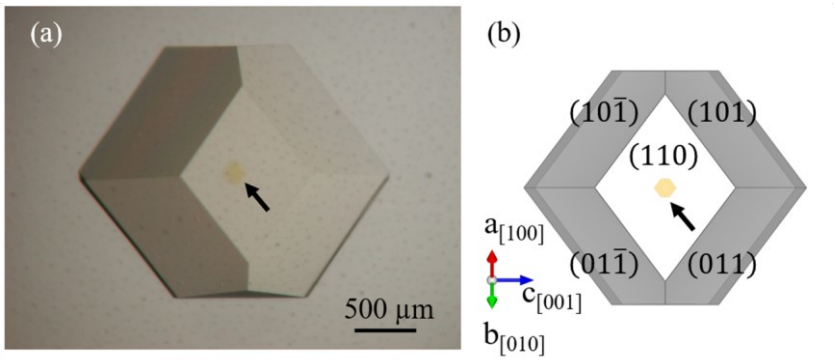

Figure A.1. (a) Optical micrograph and (b) the corresponding schematic morphology of a typical GI crystal grown by using a seed crystal cross-linked by a glutaraldehyde. The yellow contrast indicated by arrow at the center of the crystal in (a) correspond to the cross-linked seed crystal.

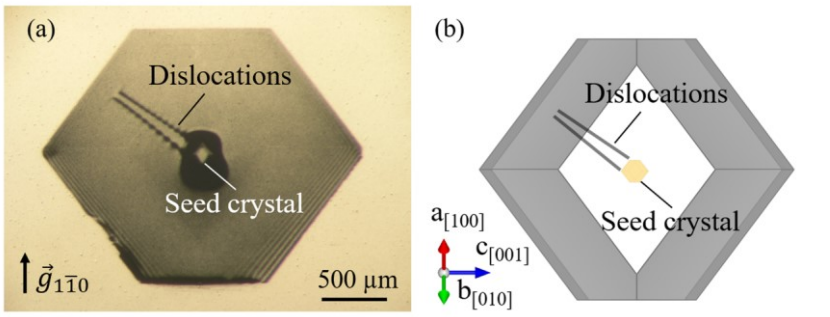

Figure A.2. (a) Synchrotron monochromatic-beam X-ray topograph of the same GI crystal as Fig. A.1, taken with $1\bar{1}0$ reflection and (b) the corresponding schematic figure of the orientation of the crystal for the topographic observation.

The circle-like contrasts at the central part of the crystal correspond to the regions at and around the seed crystal. The contrast can be attributed to the strain at the interface between cross-linked seed crystal and grown crystal. Two possibilities are suggested as the origin of strain at the interface. One is related to the surface roughness of the seed crystals and the other is to the change in the lattice constant between cross-linked seed crystal and grown (intrinsic) crystal. Actually the latter possibility cannot exclude even when the change in the lattice constant is very small as lysozyme crystals [60].

We next consider two straight line contrasts. As seen in Fig. A.2(a), it seems that two straight line contrasts originate from the interface between the seed crystal and the grown crystal. These line contrasts are considered to correspond to dislocations. The generation of dislocations at the interface can be attributed to the local stress due to the strain at the interface between cross-linked seed crystal and grown crystal as mentioned above.

Figs. A.3(a) and (b) show X-ray topographs of the same crystal as Fig. A.2, taken with $10\bar{1}$ and 011 reflections, respectively. Notably two line contrasts are invisible in $10\bar{1}$ and 011 reflections, whereas they are visible in $1\bar{1}0$ reflection as mentioned above. The invisibility of line contrasts depending on the reflection is an evidence that these are dislocation images. In addition, according to the invisibility criterion of dislocation images ($\boldsymbol{g}\cdot\boldsymbol{b}=0$; $\boldsymbol{g}$ and $\boldsymbol{b}$ are the diffraction vector and the Burgers

vector, respectively), Burgers vector of these two dislocations is determined to be $[1\bar{1}1]$. Thus, the Burgers vector of dislocations in GI crystals were experimentally determined.

Moreover, to clarify the stereoscopic directions of dislocations, more X-ray topographs of the crystal were taken from various orientations with the incident X-ray beam. Figs. A.4(a) and (b) show X-ray topographs in 101 and $01\bar{1}$ reflections for the same crystal as that in Fig. A.2, taken from different orientations from that in Fig. A.2. As the drawing of Fig. A.2(b) mentioned above, the orientations of the crystal in the topographic experiments corresponding to Figs. A.4(a) and (b) are schematically shown in Fig. A.5(a) and (b), respectively. The incident X-ray beam is in a direction almost vertical to the surface of paper in Figs. A.5(a) and (b), respectively. Therefore, the topographs in Fig. A.4 correspond to the projections of the crystal to the surface of paper in Fig. A.5. The stereoscopic topographs as seen in Figs. A.2(a) and 6.4(a) are correlated with the schematic drawings of the crystal containing dislocations in Fig. A.2(b) and A.5(a), respectively. From these correlations, the directions of the dislocation lines are identified to be parallel to $[91\bar{8}]$ and $[9\bar{1}\bar{8}]$, respectively.

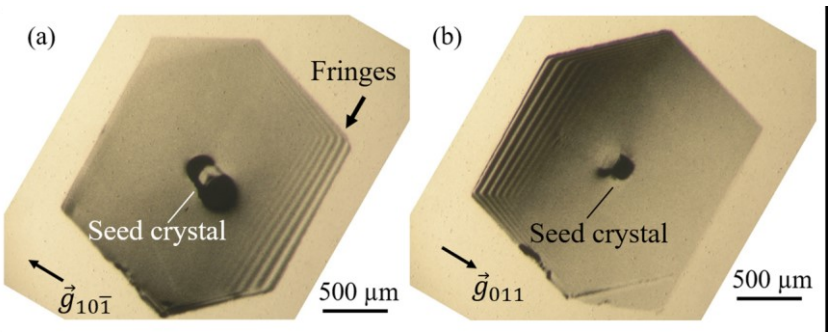

Figure A.3. Synchrotron monochromatic-beam X-ray topographs of the same GI crystal as Fig. 6.1, taken with (a) $10\bar{1}$ and (b) 011 reflections, respectively.

These directions and positions of dislocations are more clarified by the observation of etch pits. As seen in Fig. A.6, two etch pits are found to be formed on $(10\bar{1})$ surface. The positions of etch pits are in good agreement with one end points of two dislocation lines observed by X-ray topography as mentioned above. This means that etch pits are produced at the outcrops of dislocations at the $(10\bar{1})$ surface of the crystal. Thus, the dislocations emerge at $(10\bar{1})$ surface of the crystal.

The angles between Burgers vector $[1\bar{1}1]$ and dislocation lines of $[91\bar{8}]$ and $[9\bar{1}\bar{8}]$ are 94° and 89°, respectively. These directions of dislocations are almost vertical to the Burgers vector. Thus, the dislocations observed in the crystals are close to be of pure edge character. The planes including both

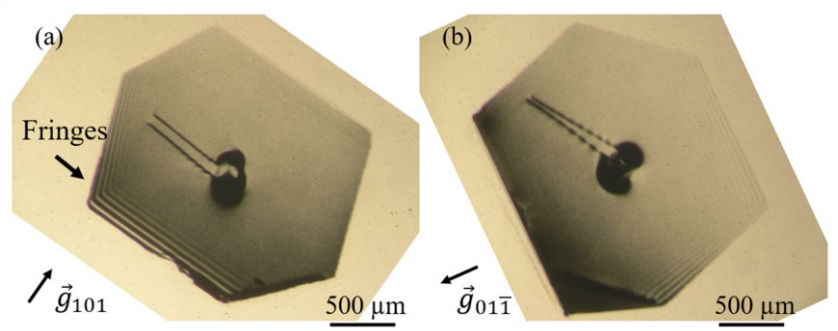

Figure A.4. Synchrotron monochromatic-beam X-ray topographs of the same GI crystal as Fig. A.1, taken with (a) 101 and (b) $01\bar{1}$ reflections, respectively.

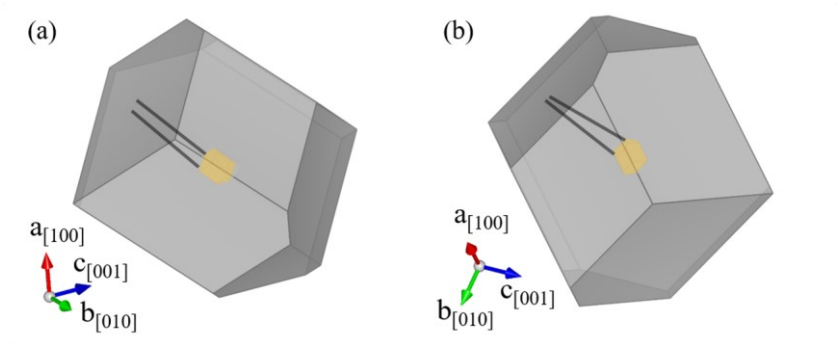

Figure A.5. Schematic figures of the orientation of the GI crystal, respectively, for topographic observations with (a) 101 and (b) $01\bar{1}$ reflections in Fig. A.4.

Burgers vector and dislocations of $[91\bar{8}]$ and $[9\bar{1}\bar{8}]$ are analyzed to be $(7\ 17\ 10)$ and $(9\ 17\ 8)$, respectively. These planes can be considered as slip planes for two dislocations. These dislocations might be generated by slip due to the local stress at the interface.

As seen in Fig. A.7, the molecular arrangement in GI crystals is close to a body-centered cubic (bcc) one, although the exact crystal structure is a body-centered orthorhombic one. Note that the molecular arrangement in Fig. A.7 was drawn by using a Mercury software [93] with Protein Data Bank (PDB)

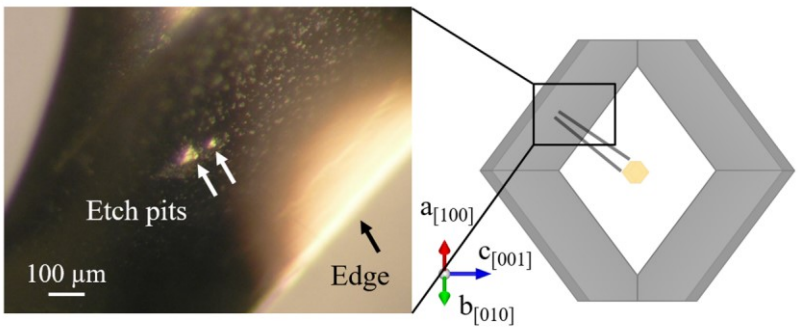

Figure A.6. Optical micrograph of two etch pits observed on $(10\bar{1})$ surface of the same GI crystal as Fig.A.1. The corresponding positions with dislocation lines in the crystal morphology are schematically shown in the left figure.

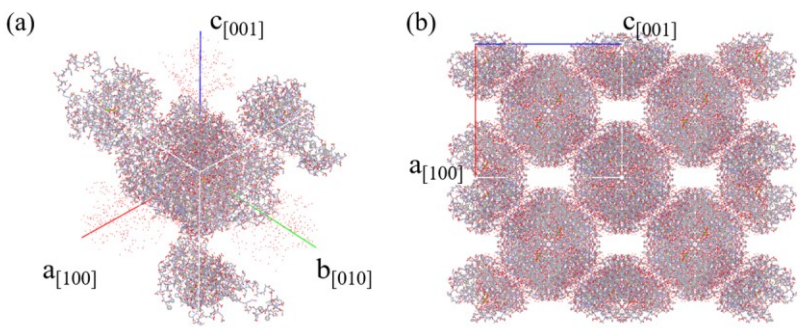

Figure A.7. Schematic figures of (a) the unit cell of GI crystals with orthorhombic structure and (b) the molecular arrangement viewed from b axis, which are close to a body-centered cubic (bcc) one. The space between molecules is occupied by mobile water.

1mnz [69] for GI crystals. Generally, in bcc metal, slip occurs in closed-packed $[111]$ directions [19,94]. The shortest lattice vector, i.e. the Burgers vector of the perfect dislocation, is of the type $1/2\langle 111\rangle$. The crystallographic slip planes are $\{110\}$, $\{112\}$ and $\{123\}$. The identified Burgers vector in GI crystal is $\langle 111\rangle$ which is in good agreement with typical one in bcc metal. On the other hand, the slip planes of $(7\ 17\ 10)$ and $(9\ 17\ 8)$ are different from typical ones in bcc metals. However, these planes are roughly parallel to (121) which is one of typical slip planes in bcc metals. In addition, edge dislocations of $[91\bar{8}]$ and $[9\bar{1}\bar{8}]$ directions in GI crystals as observed above can be correlated with that of $[10\bar{1}]$ direction in the case of bcc metals. Thus, it seems that the characteristics of dislocations in GI crystals are similar to those of typical bcc metals.

Such dislocations associated with higher-order directions and slip planes might be easily generated in protein crystals, although they can be often observed in grown-in dislocations. In recent indentation experiments for lysozyme crystals, a lot of slip systems have been observed [58]. This means that the magnitude of shear stress for slip or peierls stress in protein crystals might not be dependent on the crystallographic orientation due to the huge molecules with unique shapes and the weakness of the intermolecular interaction. Thus even higher-order planes and dislocations in GI crystals would be easily activated as slip system, as lower-order ones.

Generally, it is difficult to generate dislocations with higher-order directions and slip planes in inorganic crystals. However, dislocation lines with jogs and/or kinks can be seen along higher order

directions and planes deviating from the pure lower order ones [19,94]. For example, in Mo crystals with bcc structure by compression, a lot of kinks and jogs formed along dislocation lines have been observed by transmission electron microscopy (TEM) [95]. The dislocations with kinks and/or jogs can occupy not a 1D but 2D and 3D space in the crystal. As seen in Fig. A.8, assuming that the dislocations in GI crystals are also accompanied by kinks and jogs, the edge-like dislocations of $[91\bar{8}]$ and $[9\bar{1}\bar{8}]$ directions can be also interpreted as $[10\bar{1}]$ ones with jogs and kinks associated with (121) slip planes which are typical ones in bcc metals, although it is hard to observe the kinks and jogs at the molecular-scale in the GI crystals due to the resolution of X-ray topography lower than that of TEM observation.

Moreover, we also consider other interesting contrasts: one is fringes at crystal edges and the other is bead-like or oscillatory contrasts along straight line images corresponding to dislocations. As seen in Figs. A.2(a), A.3 and A.4, the fringes are obviously observed in all of topographs, and are appeared

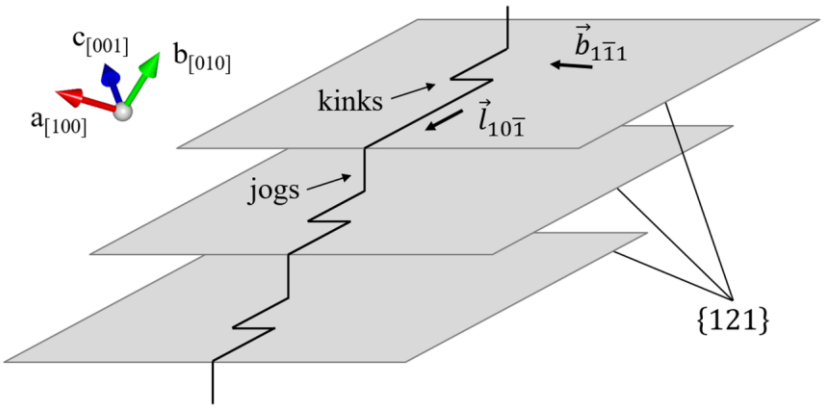

Figure A.8. Schematic figure of a dislocation line of $[10\bar{1}]$ with jogs and kinks associated with $\{121\}$ slip planes in GI crystals.

at tapered or wedge-like edges of the crystal. Such fringes have never been observed in other protein crystals such as lysozyme, ribonuclease and so far [29–44,46–48]. They can correspond to the equal-thickness fringes, related to Pendellösung fringes, due to the dynamical diffraction effect which has been often observed in only high quality crystals such as Si. In addition, the bead-like contrasts also have never been observed in other protein crystals so far, and have been often observed in high quality crystals such as Si [96]. The unique contrasts are also known as intermediary contrasts due to dynamical diffraction effect, where they arise from the interference between the new wave field created below the defect and the undeviated original wave field propagating in the perfect regions of the crystal [63,97]. Thus, it seems that the perfection of GI crystals shown in this paper is extremely high compared with other protein crystals reported so far, and is comparable to that of Si. The detailed analysis for the dynamical contrasts in GI crystals is in progress.

A.4. Conclusion

We have shown the characterization of dislocations in high-quality GI crystals by synchrotron monochromatic-beam X-ray topography. From the invisibility criterion of the dislocation images, it is experimentally determined that they are of edge character with a Burgers vector of $[1\bar{1}1]$ (b=17.1 nm). Moreover, bead-like contrasts along the dislocation images and the equal-thickness fringes, related to Pendellösung fringes, at crystal edges are clearly observed, which have never been seen in

other protein crystals so far. These contrasts can attributed to the dynamical diffraction effect which has been often observed in high-quality crystals such as Si. This means that the perfection of GI crystals is extremely high compared with other protein crystals. Thus, more features of topographic images, especially dislocation images, in protein crystals would be clarified by using the high-quality GI crystals.

Appendix B:

Performance of X-ray optical systems ~DuMond diagram~

To measure the rocking curves of the crystal, the angular resolution of the optics must be considered. The DuMond diagram [67] has been used to describe X-ray optical properties of multiple-crystal arrangements such as two-crystal monochromator. The correlation between the angle θ and wavelength λ is described using the $\theta - \lambda$ space, where θ and λ is the angle between the incident X-ray direction and the lattice plane, and the wavelength of the incident beam, respectively.

Let us consider the condition of the monochromatic beam of $\lambda = 1.0$ Å using the monochromator consisting of a Si(111) crystal. The correlation between the Bragg angle θ_B of the Si(111) and wavelength λ is shown in Figure B.1. When the incident beam satisfies the Bragg angle of the monochromator, the rocking curve of the Si(111) is described as shown in Figure B.2. This profile of rocking curve corresponds to the area A–A' in Figure B.1. The horizontal axis is the peak position which corresponds to the deviation angle from the Bragg angle θ_B. The center of the profile is

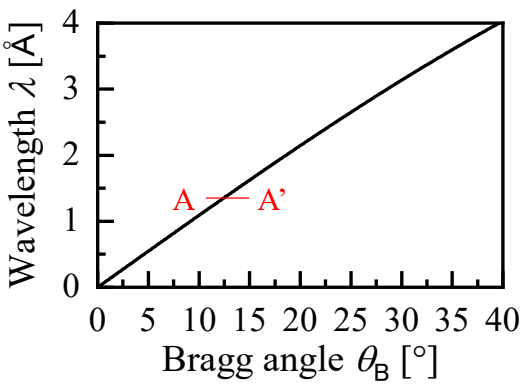

Figure B.1. The correlation between the Bragg angle θ_B of the Si(111) and wavelength λ.

deviated a little due to the reflection of X-ray with the monochromator. In the case of the diffraction with Bragg case using perfect crystal such as Si, the total reflection occurs by dynamical diffraction. The width of the total reflection ω is approximately 4.38 arcsec (1.22×10^{-3}°). Figure B.3 shows the enlarged one of the area A–A' shown in Figure B.1. The area with orange color corresponds to the total reflection one. Here, the incident beam has a divergence estimated from the geometry of the experimental system, $\Delta\theta$, which is the area with gray color as seen in Figure B.3. The overlapped area corresponds to the $\theta - \lambda$ distribution.

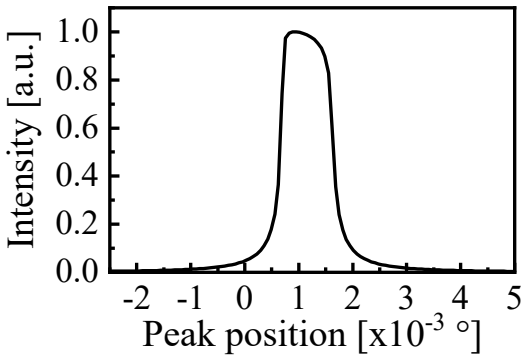

Figure B.2. The rocking curve of Bragg case for the 111 reflections of Si with an incident beam with a wavelength of 1.0 Å.

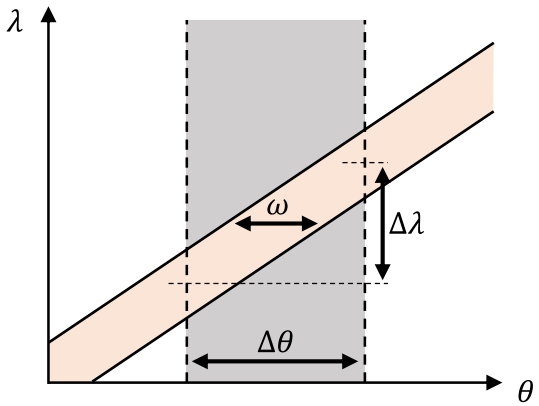

Figure B.3. The angular and wavelength divergence of the reflected X-ray.

Figure B.4 shows the correlation of the sample crystal (*e.g.* glucose isomerase (GI) crystal) between the Bragg angle θ_B and wavelength λ as Si(111). Let us consider the beam divergence when the diffraction of sample crystal occurs. Figure B.5 shows the overlapped profile of the $\theta - \lambda$ distribution with Si(111) and GI(011). This geometric figure has been called as DuMond diagram. Here d_1 and θ_1 are the plane distance and the Bragg angle of Si(111), respectively, d_1 and θ_1 are the plane distance and the Bragg angle of (011) of the GI crystal, respectively.

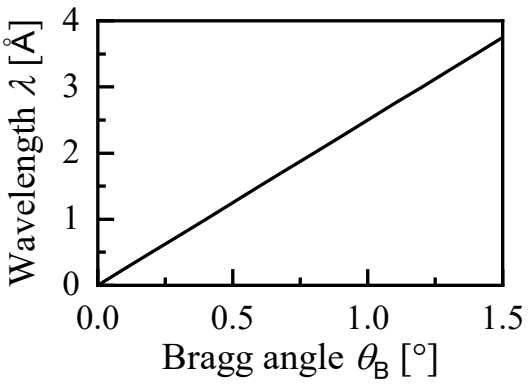

Figure B.4. The correlation between the Bragg angle θ_B of the GI(011) and the wavelength λ.

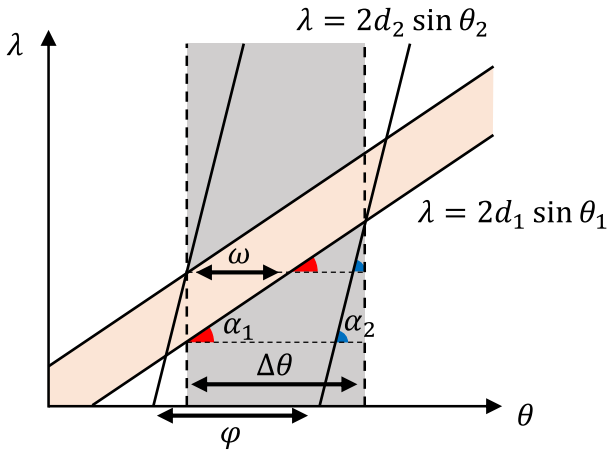

Figure B.5. The DuMond diagram

From the geometry,

$$(\Delta\theta - \varphi)\tan\alpha_2 = (\Delta\theta - \omega)\tan\alpha_1. \tag{B.1}$$

By expanding the Eq. (B.1), the angular resolution of the optics, φ, is given by

$$\varphi = \left(1 - \frac{\tan\alpha_1}{\tan\alpha_2}\right)\Delta\theta + \frac{\tan\alpha_1}{\tan\alpha_2}\omega. \tag{B.2}$$

From the Bragg equation, the slope $\frac{d\lambda}{d\theta}$ is given by

$$\frac{d\lambda}{d\theta} = 2d\cos\theta = \frac{\lambda}{\tan\theta}. \tag{B.3}$$

From the geometry, the slope is given by

$$2d_1\cos\theta_1 = \tan\alpha_1,\ 2d_2\cos\theta_2 = \tan\alpha_2, \tag{B.4}$$

respectively, too. Therefore, from the Eqs. (B.3) and (B.4),

$$\frac{\tan\alpha_1}{\tan\alpha_2} = \frac{\tan\theta_2}{\tan\theta_1}. \tag{B.5}$$

From the Eqs. (B.2) and (B.5), the angular resolution of the optics, φ, is provided by

$$\varphi = \left(1 - \frac{\tan\theta_2}{\tan\theta_1}\right)\Delta\theta + \frac{\tan\theta_2}{\tan\theta_1}\,\omega. \tag{B.6}$$

Then, let us consider the beam divergence, $\Delta\theta$, estimated from the geometry of the experimental system. Figure B.6 shows the geometric correlation of the beam divergence of the light source, H, the slit size, s, and the distance, L, between the light source and the X-ray detector. From the geometry, the correlation is given by

$$\tan\left(\frac{\Delta\theta}{2}\right) = \frac{(H+s)/2}{L}, \tag{B.7}$$

therefore,

$$\Delta\theta = 2\tan^{-1}\left(\frac{H+s}{2L}\right). \quad \text{(B.8)}$$

Here, using the vertical beam divergence of the light source, $\sigma_{y\prime}$, as Gaussian distribution, the beam divergence of the light source, H, is given by

$$H = 2\sigma_y\sqrt{2\ln 2}. \quad \text{(B.9)}$$

Therefore, the beam divergence estimated from the geometry of the experimental system, $\Delta\theta$, is given by

$$\Delta\theta = 2\tan^{-1}\left(\frac{2\sigma_y\sqrt{2\ln 2}+s}{2L}\right). \quad \text{(B.10)}$$

Finally, combining the Eqs. (B.6) and (B.10), the angular resolution of the optics, φ, is obtained as

$$\varphi = \left(1-\frac{\tan\theta_2}{\tan\theta_1}\right)\min\left[\Delta\theta, \sigma_{y'}\right] + \frac{\tan\theta_2}{\tan\theta_1}\omega. \quad \text{(B.11)}$$

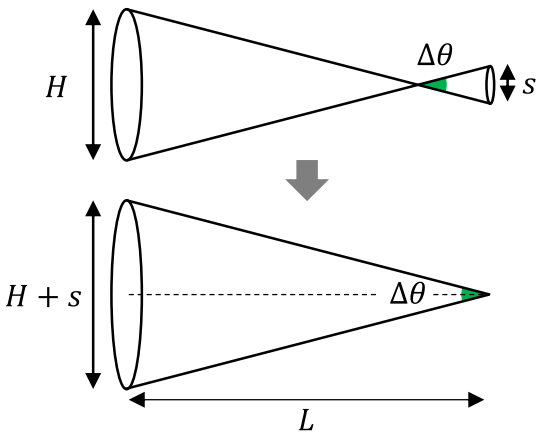

Figure B.6. Schematics of the geometry of the experimental system.

Acknowledgement

This work was carried out at the Graduate School of Nanobioscience, Yokohama City University from April 2017 to November 2018.
My gratitude is beyond the words scribbled here.

To begin with, the author would like to express his sincere appreciation and gratitude to his advisor, Prof. Masaru Tachibana for his encouragement and guidance received throughout the course of this study and for introducing his to the field of solid physics. Though it was a tough time to be a Ph.D student, the experiences are irreplaceable and precious to me.

The author would like also to express his gratitude to Prof. Kenichi Kojima for his discussion and helpful advice, without help this study far would not have been possible.

The author would like to thank Dr. Haruhiko Koizumi of Nagoya University, Dr. Kei Wako of Yokohama Soei University and Dr. Hidenobu Murata of Osaka Prefecture University for their supporting the experiments and useful discussion.

The author would like to thank Dr. Hiroshi Sugiyama and Dr. Keiichi Hirano of the Institute of Materials Structure Science for their help with the analysis and the synchrotron radiation X-ray experiments in BL-14B and BL-20B at KEK-PF.

The author would like to thank Dr. Takashi Kumasaka, Dr. Seiki Baba and Dr. Nobuhiro Mizuno of the Japan Synchrotron Radiation Research Institute for their help with the synchrotron radiation X-ray experiments in BL38B1 at SPring-8.

The author would like to thank Prof. Katsuo Tsukamoto of Osaka University, Dr. Yoshihisa Suzuki of Tokushima University, Dr. Yasutomo Arai of Japan Aerospace Exploration Agency, Mr. Seijiro Fukuyama of Advanced Engineering Services Co., Ltd. for their help with sample preparation.

The author gives his thanks to group members of Prof. M. Tachibana's laboratories for supporting his study, research and enjoying his University life.

Finally, the author would like to thank his family for supporting his life and approving continuous study.

References

[1] N.E. Chayen, J.R. Helliwell, E.H. Snell, Macromolecular Crystallization and Crystal Perfection, Oxford Univ Press, Oxford, 2010.

[2] A. McPherson, Crystallization of Biological Macromolecules, Cold Spring Harbor Laboratory Press, New York, 1999.

[3] B.W. Matthews, Solvent content of protein crystals, J. Mol. Biol. **33** (1968) 491–497.

[4] L.Z. Vilenchik, J.P. Griffith, N.S. St Clair, M.A. Navia, A.L. Margolin, Protein crystals as novel microporous materials, J. Am. Chem. Soc. **120** (1998) 4290–4294.

[5] A.L. Margolin, M.A. Navia, Protein crystals as novel catalytic materials, Angew. Chem. Int. Ed. **40** (2001) 2204–2222.

[6] S. Abe, T. Ueno, Design of protein crystals in the development of solid biomaterials, RSC Adv. **5** (2015) 21366–21375.

[7] W.H. Zachariasen, Theory of X-ray Diffraction in Crystals Dover Publications, New York, 1945.

[8] B.W. Batterman, H. Cole, Dynamical diffraction of X rays by perfect crystals, Rev. Mod. Phys. **36** (1964) 681–717.

[9] O. Brümmer, Z.G. Pinsker, Dynamical Scattering of X-Rays in Crystals, Springer, Berlin, 1978.

[10] A. Authier, Dynamical Theory of X-Ray Diffraction, Oxford Science Publications, Oxford, 2001.

[11] N. Kato, A.R. Lang, A study of Pendellösung fringes in X-ray diffraction, Acta Crystallogr. **12** (1959) 787–794.

[12] P.J.E. Aldred, M. Hart, The electron distribution in silicon. I. Experiment, Proc. R. Soc. A **332** (1973) 223–238.

[13] M. Lefeld-Sosnowska, C. Malgrange, Experimental evidence of plane wave rocking curve oscillations, Phys. Status Solidi B **34** (1969) 635–647.

[14] U. Bonse, W. Graeff, R. Teworte, H. Rauch, Oscillatory structure of Laue case rocking curves, Phys. Status Solidi A **43** (1977) 487–492.

[15] T. Ishikawa, Measurement of the coherence length of highly collimated X-rays from the visibility of equal-thickness fringes, Acta Crystallogr. A **44** (1988) 496–499.

[16] T. Ishikawa, K. Hirano, S. Kikuta, Applications of perfect crystal X-ray optics, Nucl. Instrum. Meth. A **308** (1991) 356–362.

[17] E. Persson, The Laue case of X-ray diffraction in nearly perfect germanium crystals, Phys. Scr. **3** (1971) 293–301.

[18] G. Kowalski, A.R. Lang, A.P.W. Makepeace, M. Moore, Studies of stacking-fault contrast by synchrotron X-ray section topography, J. Appl. Crystallogr. **22** (1989) 410–430.

[19] J.P. Hirth, J. Lothe, Theory of Dislocations, second ed., Wiley, New York, 1982.

[20] J.O. Williams, J.M. Thomas, Lattice imperfections in organic solids. Part 1. e Anthracene, Trans. Faraday Soc. **63** (1967) 1720–1729.

[21] M. Tachibana, K. Kono, M. Shimizu, K. Kojima, Growth and dislocation characteristics of organic molecular crystals: 2,3-dimethylnaphrhalene, J. Cryst. Growth **198/199** (1999) 665–669.

[22] V. Vitek, V. Paidar, Non-planar dislocation cores: a ubiquitous phenomenon affecting mechanical properties of crystalline materials, Dislocation in Solids **14** (2008) 441–538.

[23] M.A. Meyers, K.K. Chawla, Mechanical Behavior of Materials, second ed., Cambridge University Press, Cambridge, 2008.

[24] M.S.R.N. Kiran, S. Varughese, U. Ramamurty, G.R. Desiraju, Effect of dehydration on the mechanical properties of sodium saccharin dihydrate probed with nanoindentation, CrystEngComm **14** (2012) 2489–2493.

[25] S. Mannepalli, K.S.R.N. Mangalampalli, Indentation plasticity and fracture studies of organic crystals, Crystals **7** (2017) 324.

[26] B.K. Tanner, X-ray Diffraction Topography, Pergamon Press, Oxford, 1976.

[27] H. Klapper, H.C. Freyhardt (Ed.)Crystals 13, Springer, Berlin, 1991, pp. 109–164.

[28] D.K. Bowen, B.K. Tanner, High-Resolution X-Ray Diffractometry and Topography, Taylor & Frances, London, 1998.

[29] R. Fourme, A. Ducrulx, M. Ries-Kautt, B. Capelle, The Perfection of Protein Crystals Probed by Direct Recording of Bragg Reflection Profiles with a Quasi-Planar X-ray Wave, J. Synchrotron Rad. **2** (1995) 136–142.

[30] V. Stojanoff, D.P. Siddons, X-ray topography of a lysozyme crystal, Acta Cryst. **A52** (1996) 498–499.

[31] K. Izumi, S. Sawamura, M. Ataka, X-ray topography of lysozyme crystals, J. Cryst. Growth **168** (1996) 106–111.

[32] V. Stojanoff, D.P. Siddons, L.A. Monaco, P. Vekilov, F. Rosenberger, X-ray topography of tetragonal lysozyme grown by the temperature-controlled technique, Acta Cryst. **D53** (1997) 588–595.

[33] I. Dobrianov, K.D. Finkelstein, S.G. Lemay, R.E. Thorne, X-ray topographic studies of protein crystal perfection and growth, Acta Cryst. **D54** (1998) 922–937.

[34] F. Otalora, J.M. Garcia-Ruiz, J.A. Gavira, B. Capelle, Topography and high resolution diffraction studies in tetragonal lysozyme, J. Cryst. Growth **196** (1999) 546–558.

[35] K. Izumi, K. Taguchi, Y. Kobayashi, M. Tachibana, K. Kojima, M. Ataka, Screw dislocation lines in lysozyme crystals observed by Laue topography using synchrotron radiation, J. Cryst. Growth **206** (1999) 155–158.

[36] T.J. Boggon, J.R. Helliwell, R.A. Judge, A. Olczak, D.P. Siddons, E.H. Snell, V. Stojanoff, Synchrotron X-ray reciprocal-space mapping, topography and diffraction resolution studies of macromolecular crystal quality, Acta Cryst. **D56** (2000) 868–880.

[37] Z.W. Hu, B.R. Thomas, A.A. Chernov, Laboratory multiple-crystal X-ray topography and reciprocal-space mapping of protein crystals: influence of impurities on crystal perfection, Acta Cryst. **D57** (2001) 840–846.

[38] Z.W. Hu, B. Lai, Y.S. Chu, Z. Cai, D.C. Mancini, B.R. Thomas, A.A. Chernov, Phase sensitive X-ray diffraction imaging of defects in biological macromolecular crystals, Phys. Rev. Lett. **87** (2001) 148101.

[39] W.M. Vetter, D.T. Gallagher, M. Dudley, Synchrotron white-beam X-ray topography of ribonuclease S crystals, Acta Cryst. **D58** (2002) 579–584.

[40] M. Tachibana, H. Koizumi, K. Izumi, K. Kajiwara, K. Kojima, Identification of dislocations in large tetragonal hen egg-white lysozyme crystals by synchrotron white-beam topography., J. Synchrotron Rad. **10** (2003) 416–420.

[41] D.T. Gallagher, C. Stover, D. Charlton, L. Arnowitz, D.R. Blacka, X-ray topography of microgravity-grown ribonuclease S crystals, J. Cryst. Growth **255** (2003) 403–413.

[42] Z.W. Hu, Y.S. Chu, B. Lai, B.R. Thomas, A.A. Chernov, Diffraction and imaging study of imperfections of crystallized lysozyme with coherent X-rays, Acta Cryst. **D60** (2004) 621–629.

[43] B. Capelle, Y. Epelboin, J. Härtwig, A.B. Moraleda, F. Otálora, V. Stojanoff, Characterization of dislocations in protein crystals by means of synchrotron double-crystals topography, J. Appl. Cryst. **37** (2004) 67–71.

[44] H. Koizumi, M. Shimizu, M. Tachibana, K. Kojima, Characterization of dislocations in orthorhombic hen egg-white lysozyme crystals by synchrotron X-ray topography, Phys. Status Solidi A **204** (2007) 2688–2693.

[45] B.K. Tanner, Dislocation contrast in X-ray topographs of very thin crystals, Phys. Status Solidi A **10** (1972) 381–386.

[46] M. Koishi, N. Ohya, Y. Mukobayashi, H. Kitajima, H. Koizumi, K. Kojima, M. Tachibana, Observation of clear images of dislocations in protein crystals by synchrotron monochromatic-beam X-ray topography, Cryst. Growth Des. **7** (2007) 2182–2186.

[47] Y. Mukobayashi, N. Kitajima, Y. Yamamoto, K. Kajiwara, H. Sugiyama, K. Hirano, K. Kojima, M. Tachibana, Observation of dislocations in hen egg-white lysozyme crystals by synchrotron monochromatic-beam X-ray topography., Phys. Status Solidi A **206** (2009) 1825‑1828.

[48] T. Sawaura, D. Fujii, M. Shen, Y. Yamamoto, K. Wako, K. Kojima, M. Tachibana, Characterization of dislocations in monoclinic hen egg-white lysozyme crystals by synchrotron monochromatic-beam X-ray topography, J. Cryst. Growth **318** (2011) 1071–1074.

[49] H. Koizumi, R. Suzuki, M. Tachibana, K. Tsukamoto, I. Yoshizaki, S. Fukuyama, Y. Suzuki, S. Uda, K. Kojima, Importance of determination of crystal quality in protein crystals when performing high-resolution structural analysis, Cryst. Growth Des. **16** (2016) 4905–4909.

[50] R. Suzuki, H. Koizumi, K. Kojima, S. Fukuyama. Y. Aarai, K. Tsukamoto, Y. Suzuki, M. Tachibana, Characterization of grown-in dislocations in high-quality glucose isomerase crystals by synchrotron monochromatic-beam X-ray topography, J. Cryst. Growth **468** (2017) 299–304.

[51] J.R. Helliwell, Protein crystal perfection and the nature of radiation damage, J. Cryst. Growth **90** (1988) 259–272.

[52] E.H. Snell, S. Weisgerber, J.R. Helliwell, K. Hölzer, K. Schroer, Improvements in lysozyme protein crystal perfection through microgravity growth, Acta Cryst. **D51** (1995) 1099–1102.

[53] H.M. Volz, R.J. Matyi, Triple-axis X-ray diffraction analyses of lysozyme crystals, Acta Cryst. **D56** (2000) 881–889.

[54] D. Lübbert, A. Meents, E. Weckert, Accurate rocking-curve measurements on protein crystals grown in a homogeneous magnetic field of 2.4 T, Acta Cryst. **D60** (2004) 987–998.

[55] M. Tachibana, Y. Kobayashi, T. Shimazu, M. Ataka, K. Kojima, Growth and mechanical properties of lysozyme crystals, J. Cryst. Growth **198/199** (1999) 661–664.

[56] H. Koizumi, M. Tachibana, H. Kawamoto, K. Kojima, Temperature dependence of microhardness of tetragonal hen-egg-white lysozyme single crystals, Phil. Mag. **84** (2004) 2961–2968.

[57] H. Koizumi, H. Kawamoto, M. Tachibana, K. Kojima, Effect of intracrystalline water on micro-Vickers hardness in tetragonal hen egg-white lysozyme single crystals, J. Phys. D **41** (2008) 074019.

[58] R. Suzuki, T. Kishi, S. Tsukashima, M. Tachibana, K. Wako, K. Kojima, Hardness and slip systems of orthorhombic hen egg-white lysozyme crystals, Phil. Mag. **96** (2016) 2930–2942.

[59] T. Kishi, R. Suzuki, C. Shigemoto, H. Murata, K. Kojima, M. Tachibana, Microindentation hardness of protein crystals under controlled relative humidity, Crystals **7** (2017), 339.

[60] H. Koizumi, M. Tachibana, K. Kojima, Elastic constants in tetragonal hen egg-white lysozyme crystals containing large amount of water, Phys. Rev. E **79** (2009) 061917.

[61] N. Kitajima, S. Tsukashima, D. Fujii, M. Tachibana, H. Koizumi, K. Wako, K. Kojima, Elastic constants in orthorhombic hen egg-white lysozyme crystals, Phys. Rev. E **89** (2014) 012714.

[62] J.R. Helliwell, Macromolecular Crystallography with Synchrotron Radiation, Cambridge Univ Press, Cambridge, 2005.

[63] B. Raghothamachar, G. Dhanaraj, J. Bai, M. Dudley, Defect analysis in crystals using X-ray topography, Microsc. Res. Tech. **69** (2006) 343–358.

[64] H.L. Carrell, J.P. Glusker, V. Burger, F. Manfre, D. Tritsch, J. Biellmann, X-ray analysis of D-xylose isomerase at 1.9 Å: native enzyme in complex with substrate and with a mechanism-designed inactivator, Proc. Natl. Acad. Sci. USA **86** (1989) 4440–4444.

[65] R.L. Owen, N. Paterson, D. Axford, J. Aishima, C. Schulze-Briese, J. Ren, E.E. Fry, D.I, Stuart, G. Evans, Exploiting fast detectors to enter a new dimension in room-temperature crystallography, Acta Crys. **D70** (2014) 1248–1256.

[66] F. Stellato, D. Oberthür, M. Liang, R. Bean, C. Gati, O. Yefanov, A. Barty, A. Burkhardt, P. Fischer, L. Galli, R.A. Kirian, J. Meyer, S. Panneerselvam, C.H. Yoon, F. Chervinskii, E. Speller, T.A. White, C. Betzel, A. Meentsc, H.N. Chapman, Room-temperature macromolecular serial crystallography using synchrotron radiation, IUCrJ **1** (2014) 204–212.

[67] J.W.N. DuMond, Theory of the use of more than two successive X-ray crystal reflections to obtain increased resolving power, Phys. Rev. **52** (1937) 872–883.

[68] KEK, Part A: Highlights and Facility Report. Photon Factory Activity Report, KEK, Ibaraki, Japan, **32** (2014) 65–67.

[69] E. Nowak, S. Panjikar, P.A. Tucker, Atomic structure of glucose isomerase, (2002) Available at https://www.rcsb.org/structure/1MNZ. Accessed March 12, 2018.

[70] M.K. Gilson, B.H. Honig, The dielectric constant of a folded protein, Biopolymers **25** (1986) 2097–2119.

[71] T. Simonson, Brooks CL, Charge screening and the dielectric constant of proteins: Insights from molecular dynamics, J. Am. Chem. Soc. **118** (1996) 8452–8458.

[72] L.N. Rashkovich, V.A. Smirnov, E.V. Petrova, Some dielectric properties of monoclinic lysozyme crystals, Phys. Solid State **50** (2008) 631–637.

[73] Y. Hirano, K. Takeda, K. Miki, Charge-density analysis of an iron-sulfur protein at an ultra-high resolution of 0.48 Å, Nature **534** (2016) 281–284.

[74] M. Hart, 'Perfect' crystals in crystal structure analysis, Acta Cryst. **B51** (1995) 483–485.

[75] H. Wolf, M.R.V. Jørgensen, Y.S Chen, R. Herbst-Irmer, D. Stalke, Charge density investigations on [2,2]-paracyclophane–In data we trust, Acta Cryst. **B71** (2015) 10–19.

[76] K. Momma, F. Izumi, VESTA 3 for three-dimensional visualization of crystal, volumetric and morphology data, J. Appl. Crystallogr. **44** (2011) 1272–1276.

[77] G. Otting, E. Liepinsh, K. Wuthrich, Protein hydration in aqueous solution, Science **254** (1991) 974–980.

[78] V.N. Morozov, G.S. Kachalova, V.U. Evtodienko, N.F. Lanina, T.Y. Morozova, Permeability of lysozyme tetragonal crystals to water, Eur. Biophys. J. **24** (1995) 93–98.

[79] M.J. Jones, J. Ulrich, Are different protein crystal modifications polymorphs? A discussion, Chem. Eng. Technol. **33** (2010) 1571–1576.

[80] S.K. Pal, A.H. Zewail, Dynamics of water in biological recognition, Chem. Rev. **104** (2004) 2099–2123.

[81] P.G. Vekilov, What is the molecular-level role of the solution components in protein crystallization? Cryst. Growth Des. **7** (2007) 2239–2246.

[82] J.J. Gilman, Chemistry and Physics of Mechanical Hardness, first ed., John Wiley and Sons, Hoboken, 2009.

[83] M. Tachibana, H. Sakuma, K. Kojima, Photo-illumination hardening of C60 crystals, J. Appl. Phys. **82** (1997) 4253–4258.

[84] A. Zamiri, S. De, Modeling the mechanical response of tetragonal lysozyme crystals, Langmuir **26** (2010) 4251–4257.

[85] S. Tait, E.T. White, J.D. Litster, Mechanical characterization of protein crystals, Part. Part. Syst. Char. **25** (2008) 266–276.

[86] C.N. Nanev, I. Dimitrov, D. Tsekova, Adhesion of protein crystals: measurement of the detachment force, Cryst. Res. Technol. **41** (2006) 505–509.

[87] C.N. Nanev, Brittleness of protein crystals, Cryst. Res. Technol. **47** (2012) 922–927.

[88] H. Koizumi, M. Tachibana, I. Yoshizaki, S. Fukuyama, K. Tsukamoto, Y. Suzuki, S. Uda, K. Kojima, Dislocations in high-quality glucose isomerase crystals grown from seed crystals, Cryst. Growth Des. **14** (2014) 5111–5116.

[89] R. Suzuki, H. Koizumi, K. Hirano, T. Kumasaka, K. Kojima, M. Tachibana, Analysis of oscillatory rocking curve by dynamical diffraction in protein crystals, Proc. Natl. Acad. Sci. U.S.A. **115** (2018) 3634–3639.

[90] A.M. Minor, E.T. Lilleodden, M. Jin, E.A. Stach, D.C. Chrzan, J.W. Morris Jr., Room temperature dislocation plasticity in silicon, Phil. Mag. **85** (2005) 323–330.

[91] D.A. Jones, J.W. Mitchell, Observations on helical dislocations in crystals of silver chloride, Phil. Mag. **3** (1958) 1–7.

[92] J. Friedel, Dislocations, Elsevier, 2013.

[93] C.F. Macrae, I.J. Bruno, J.A. Chisholm, P.R. Edgington, P. McCabe, E. Pidcock, L. Rodriguez-Monge, R. Taylor, J. van de Streek, P.A. Wood, Mercury CSD 2.0 - new features for the visualization and investigation of crystal structures, J. Appl. Cryst. **41** (2008) 466–470.

[94] D. Hull, D.J. Bacon, Introduction to Dislocations, fifth ed., Butterworth-Heinemann, Oxford, 2011.

[95] L.L. Hsiung, On the mechanism of anomalous slip in bcc metals, Mat. Sci. Eng. A-Struct. **528** (2010) 329–337.

[96] H. Hattori, H. Kuriyama, N. Kato, Effects of X-Ray Polarization on Pendellösung Fringes J. Phys. Soc. Jpn. **20** (1965) 1047–1050.

[97] J.E.A. Miltat, D.K. Bowen, On the widths of dislocation images in X-ray topography under low-absorption conditions, J. Appl. Cryst. **8** (1975) 657–669.

[98] W.P. Burmeister, Structural changes in a cryo-cooled protein crystal owing to radiation damage, Acta Cryst. **D56** (2000) 328–341.

[99] N. Shimizu, K. Hirata, K. Hasegawa, G. Ueno, M. Yamamoto, Dose dependence of radiation damage for protein crystals studied at various X-ray energies J. Synchrotron Rad. **14** (2007) 4–10.

[100] H.D. Coughlan, C. Darmanin, N.W. Phillips, F. Hofmann, J.N. Clark, R.J. Harder, D.J. Vine, B. Abbey, Radiation damage in a micron-sized protein crystal studied via reciprocal space mapping and Bragg coherent diffractive imaging, Struct. Dyn. **2** (2015) 041704.

[101] O. Carugo, How large B-factors can be in protein crystal structures, BMC Bioinformatics **19** (2018) 61.